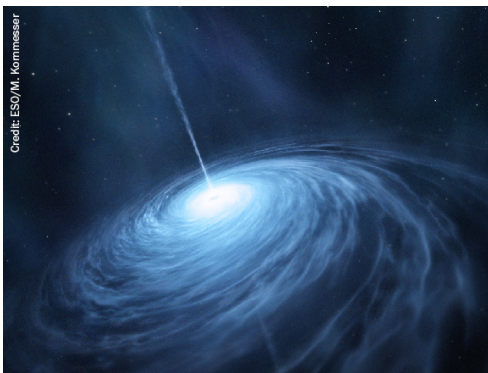**PAPER • OPEN ACCESS**

ELGAR—a European Laboratory for Gravitation and Atom-interferometric Research

To cite this article: B Canuel *et al* 2020 *Class. Quantum Grav.* **37** 225017

View the article online for updates and enhancements.

ELGAR—a European Laboratory for Gravitation and Atom-interferometric Research

B Canuel[1,*] , S Abend[2] , P Amaro-Seoane[3,4,5,6],
F Badaracco[7,8] , Q Beaufils[9], A Bertoldi[1] , K Bongs[10],
P Bouyer[1] , C Braxmaier[11,12], W Chaibi[13], N Christensen[13],
F Fitzek[2,14], G Flouris[15], N Gaaloul[2] , S Gaffet[16],
C L Garrido Alzar[9] , R Geiger[9] , S Guellati-Khelifa[17],
K Hammerer[14], J Harms[7,8] , J Hinderer[18], M Holynski[10],
J Junca[1], S Katsanevas[19], C Klempt[2], C Kozanitis[15],
M Krutzik[20], A Landragin[9] , I Làzaro Roche[16],
B Leykauf[20] , Y-H Lien[10], S Loriani[2] , S Merlet[9],
M Merzougui[13], M Nofrarias[21,22] , P Papadakos[15,23] ,
F Pereira dos Santos[9] , A Peters[20] , D Plexousakis[15,23],
M Prevedelli[24] , E M Rasel[2], Y Rogister[18], S Rosat[18] ,
A Roura[25] , D O Sabulsky[1] , V Schkolnik[20],
D Schlippert[2] , C Schubert[2,31], L Sidorenkov[9] ,
J-N Siemß[2,14] , C F Sopuerta[21,22] , F Sorrentino[26],
C Struckmann[2], G M Tino[27] , G Tsagkatakis[15,23],
A Viceré[28,29] , W von Klitzing[30], L Woerner[11,12] and
X Zou[1]

[1] Univ. Bordeaux, CNRS, IOGS, LP2N, UMR 5298,F-33400 Talence, France
[2] Leibniz Universität Hannover, Institut für Quantenoptik, Welfengarten 1, D-30167 Hannover, Germany
[3] Universitat Politècnica de València, IGIC, Spain
[4] Kavli Institute for Astronomy and Astrophysics, Beijing 100871, China
[5] Institute of Applied Mathematics, Academy of Mathematics and Systems Science, CAS, Beijing 100190, People's Republic of China
[6] Zentrum für Astronomie und Astrophysik, TU Berlin, Hardenbergstraße 36, 10623 Berlin, Germany
[7] Gran Sasso Science Institute (GSSI), I-67100 L'Aquila, Italy
[8] INFN, Laboratori Nazionali del Gran Sasso, I-67100 Assergi, Italy
[9] SYRTE, Observatoire de Paris, Université PSL, CNRS, Sorbonne Université, LNE, 61 avenue de l'Observatoire, 75014 Paris, France

[31]Current address: German Aerospace Center (DLR), Institute for Satellite Geodesy and Inertial Sensing, c/o Leibniz Universität Hannover, DLR-SI, Callinstraße 36, 30167 Hannover, Germany.
*Author to whom any correspondence should be addressed.

[10] Midlands Ultracold Atom Research Centre, School of Physics and Astronomy, University of Birmingham, Birmingham, B15 2TT, United Kingdom

[11] ZARM, Unversity of Bremen, Am Fallturm 2, 28359 Bremen, Germany

[12] DLR, German Aerospace Center, Linzer Strasse 1, 28359 Bremen, Germany

[13] ARTEMIS, Université Côte d'Azur, Observatoire de la Côte d'Azur, CNRS, F-06304 Nice, France

[14] Institute for Theoretical Physics and Institute for Gravitational Physics (Albert-Einstein-Institute), Leibniz University Hannover, Appelstrasse 2, 30167 Hannover, Germany

[15] Institute of Computer Science, Foundation for Research and Technology—Hellas, 70013, Heraklion, Greece

[16] LSBB, Laboratoire Souterrain Bas Bruit, CNRS, Avignon University—La grande combe, 84400 Rustrel, France

[17] Laboratoire Kastler Brossel, Sorbonne Université, CNRS, ENS-PSL Research University, Collège de France, 4 place Jussieu, 75005 Paris, France

[18] Institut de Physique du Globe de Strasbourg, UMR 7516, Université de Strasbourg/EOST, CNRS, 5 rue Descartes, 67084 Strasbourg, France

[19] European Gravitational Observatory (EGO), I-56021 Cascina (Pi), Italy

[20] Humboldt-Universität zu Berlin, Institut für Physik, Newtonstraße 15, 12489 Berlin, Germany

[21] Institute of Space Sciences (ICE, CSIC), Campus UAB, Carrer de Can Magrans s/n, 08193 Cerdanyola del Vallès (Barcelona), Spain

[22] Institute of Space Studies of Catalonia (IEEC), Carrer del Gran Capità, 2-4, Edifici Nexus, despatx 201, 08034 Barcelona, Spain

[23] Computer Science Department, University of Crete, 70013, Heraklion, Greece

[24] Dept. of Physics and Astronomy, Univ. of Bologna, Via Berti-Pichat 6/2, I-40126 Bologna, Italy

[25] Institute of Quantum Technologies, German Aerospace Center (DLR), Söflinger Str. 100, 89077 Ulm, Germany

[26] Istituto Nazionale di Fisica Nucleare (INFN) Sezione di Genova, via Dodecaneso 33, Genova, Italy

[27] Dipartimento di Fisica e Astronomia and LENS Laboratory, Università di Firenze and INFN-Sezione di Firenze, via Sansone 1, Sesto Fiorentino, Italy

[28] Università degli Studi di Urbino 'Carlo Bo', I-61029 Urbino, Italy

[29] INFN, Sezione di Firenze, I-50019 Sesto Fiorentino, Firenze, Italy

[30] Institute of Electronic Structure and Laser, Foundation for Research and Technology - Hellas, 70013, Heraklion, Greece

E-mail: benjamin.canuel@institutoptique.fr

CrossMark

Abstract

Gravitational waves (GWs) were observed for the first time in 2015, one century after Einstein predicted their existence. There is now growing interest to extend the detection bandwidth to low frequency. The scientific potential of multi-frequency GW astronomy is enormous as it would enable to obtain a more complete picture of cosmic events and mechanisms. This is a unique and entirely new opportunity for the future of astronomy, the success of which depends upon the decisions being made on existing and new infrastructures. The prospect of combining observations from the future space-based instrument

LISA together with third generation ground based detectors will open the way toward multi-band GW astronomy, but will leave the infrasound (0.1–10 Hz) band uncovered. GW detectors based on matter wave interferometry promise to fill such a sensitivity gap. We propose the European Laboratory for Gravitation and Atom-interferometric Research (ELGAR), an underground infrastructure based on the latest progress in atomic physics, to study space–time and gravitation with the primary goal of detecting GWs in the infrasound band. ELGAR will directly inherit from large research facilities now being built in Europe for the study of large scale atom interferometry and will drive new pan-European synergies from top research centers developing quantum sensors. ELGAR will measure GW radiation in the infrasound band with a peak strain sensitivity of $3.3 \times 10^{-22}/\sqrt{\text{Hz}}$ at 1.7 Hz. The antenna will have an impact on diverse fundamental and applied research fields beyond GW astronomy, including gravitation, general relativity, and geology.

(Some figures may appear in colour only in the online journal)

Introduction

The first confirmed observation of gravitational waves (GWs) [1] opened a new window into the study of the Universe by accessing signals and revealing events hidden to standard observatories, i.e. electromagnetic [2] and neutrino [3] detectors. Since then, several violent cosmological events have been reported, in detail ten binary black hole (BH) mergers and a binary neutron star (BNS) inspiral [4]. Moreover, the complimentary information provided by GW astronomy could, for example, bring new insight for the study of dark matter (DM) or the exploration of the early Universe, where light propagation was impossible. Expected sources of GWs range from well understood phenomena, such as the merging of neutron stars or BHs [5], to more speculative ones, such as cosmic strings [6] or early Universe phase transitions [7].

The era of GW astronomy was opened by the 'second' generation of laser interferometers LIGO [8] and VIRGO [9] that operate in a frequency band ranging from 10 Hz to 10 kHz. Other instruments operating in different frequency ranges are now required to expand the breadth of GW astronomy. Exploring the Universe with GWs from low to high frequencies (mHz to kHz) can render possible the discovery of new sources of GWs. This is a unique opportunity to expand our knowledge of the laws of nature, cosmology, and astrophysics [10]. The success of future GW astronomy depends on the choice of low frequency GW detectors. The proposal to construct the space-based Laser Interferometer Space Antenna (LISA) [11] to investigate GWs sources at very low frequency, combined with the planned third generation ground-based laser interferometer (Einstein Telescope—ET) [12] will contribute to 'multiband GW astronomy', but will leave the infrasound (0.1–10 Hz) band uncovered. An infrasound GW detector is critical to the completion of available and considered observation windows in GW astronomy [5, 13–15]; such instrument could help answer long-standing questions of cosmology involving dark energy, the equivalence principle, cosmic inflation, and the grand unified theory.

The European Laboratory for Gravitation and Atom-interferometric Research (ELGAR) proposes matter-wave interferometry to fill the sensitivity gap in this mid-band. One century after the discovery of quantum mechanics and general relativity, advanced concepts have

resulted in dramatic progress in our ability to control matter at the quantum level. Manipulating atoms at a level of coherence that allows for precise measurement has led to the development of extremely sensitive inertial sensing devices that measure, with high accuracy and precision, accelerations [16, 17], rotations [18–20], and even the tidal force induced by the spacetime curvature [21]. The outstanding performances of inertial atom sensors motivate the surge of atom interferometer (AI) experiments both in fundamental physics—e.g., to measure fundamental constants [22, 23], test general relativity [24–29], and set limits on dark energy forces [30–32]—and in applied contexts [33]—e.g., space geodesy [34], geophysics [35–37], and inertial navigation [38, 39]. Triggered by the latest progress in this field, ELGAR will use a large scale, multidimensional array of correlated AIs in free fall [40]. In such a scheme, the GW signal is obtained by an a set of differential measurements between the different matter wave interferometers, providing a strong immunity to seismic noise and an important rejection of Newtonian noise (NN), i.e. two of the most important effects impacting the performances of infrasound GW detectors.

The future infrastructure will not only fill the gap of infrasound GW observation, but could also have applications in other research domains including fundamental physics, gravitation, general relativity, and geology. ELGAR will monitor the evolution of Earth's gravitational field and rotation rate in three dimensions, thus improving our understanding of geophysical fluctuations of Earth's local gravitational field, as well as our knowledge of slow variations in gravity gradients and rotations. The data produced by ELGAR could allow empirical tests of fundamental theories of physics with unprecedented precision. For example, precise time-mapping of the fluctuation of gravitational forces could provide limits on the violations of Lorentz invariance [41] and an improved understanding of gravitational quantum mechanics [42–45]. The precise monitoring of Earth's rotation could also shed light on the Lense–Thirring effect [46], one of the many effects predicted by general relativity [24].

This paper is organized as follows: section 1 first introduces the measurement concept of large-scale atom interferometry. It then details the ELGAR geometry, derives its sensitivity to GWs and noise sources, and finally presents its main technological bricks. Section 2 presents the operating parameters and the sensitivity curve of the antenna and discuss its complementary with other GW detector projects. Section 3 then studies the new possibilities offered by ELGAR for astrophysics, gravity and fundamental physics.

1. Detector configuration and signal extraction

1.1. Atom interferometry

An AI utilizes matter-wave beam splitters and mirrors to create a quantum mechanical analog to an optical interferometer [47]. Atom interferometric techniques take advantage of a fundamental property of quantum mechanics, interference, to offer unparalleled sensitivity to changes in space–time. Here, we briefly introduce atom interferometry before delving into more details in later sections.

The atomic wave-function needs to be split, deflected, and recombined in order to observe interference, just like an electromagnetic wave in an optical interferometer. After splitting, the atomic wave-packet follows a superposition of two different paths and the interference pattern obtained after its recombination is a function of the relative phase shift accumulated along the paths. This phase shift is the result of free evolution of the atomic wave-function along each path [48]. We focus our attention on light pulse AIs, where the interrogation of the atoms for splitting, deflecting, and recombining is accomplished using coherent pulses of laser light [49]. The space–time diagram in figure 1 shows a schematic version of this process for a
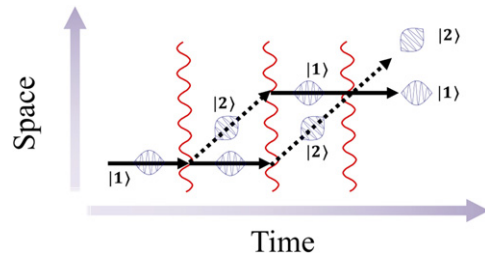
Figure 1. Space–time diagram schematic of an AI using light pulses. The atomic trajectories are represented in black: the solid lines refer to the propagation in state $|1\rangle$, the dashed ones in state $|2\rangle$. The propagation paths are represented as straight lines, whereas uniform gravity makes them parabolic. The two states have a momentum separation given by the two-photon momentum exchange imparted by the interferometric pulses, represented by the sinusoidal red lines.

single atom. An AI of this type measures the motion of the atomic wave-function relative to the reference frame defined by the laser phase fronts. This has made light pulse atom interferometry a platform for inertial sensors that offers unparalleled precision and accuracy [50]. Sensitivity to GWs is intrinsically linked to the response of an AI to the local phase of the manipulating optical field: the GW induces a variation of the travel time of photons between the atom and the laser [51].

The measurement of the AI phase requires a number of steps including preparation of the atomic sample, coherent manipulation of the matter waves which defines the instrument geometry and sensitivity, and finally detection of the output ports. Restricting our discussion to AIs using cold atom in free-fall [49], sample preparation requires collecting a dilute cloud of cold atoms, prepared with standard laser cooling and trapping techniques [52]. Using ensembles with a small spread of momenta around their center-of-mass velocity ensures that atoms travel along the intended trajectory and avoids introducing spurious signals or reducing the interferometric contrast. After the cooling phase, these ensembles are transferred into the interferometer region by launching them onto a ballistic trajectory, accomplished via a moving molasses [53], coherent momentum transfer from laser light [54, 55], or by simply dropping them. This transfer allows for the separation of the interferometric region from the atomic source, and in turn to optimize several parameters like vacuum pressure and optical access, independently. In the interferometer zone, a sequence of light pulses is applied to the atomic ensemble, to coherently divide, deflect, and finally recombine the wave-functions. The light pulses are functionally made into beam splitters or mirrors based on the amount of time in which they shine the atomic ensembles. While illuminating the atoms, the resonant electromagnetic field introduces coherent transitions between different atomic states, so-called Rabi oscillations. A beam splitter is realized for the pulse time corresponding to the creation of a superposition of states with equal probability, obtained at a fourth of a Rabi period and thus called a $\pi/2$ pulse. In a similar way, a π pulse corresponds to a flipping of the atom states and to the realization of a mirror for the matter-waves. The interrogation sequence—defining the succession of π and $\pi/2$ pulses and their distance in time—together with the direction of light with respect to the atom trajectory will define the sensitivity of the AI.

We now focus on techniques suitable to the ELGAR project. The antenna uses various laser cooling techniques for an all-optical production of atom ensembles with a 3D kinetic temperature below 1 μK, while maintaining a density dilute enough to mitigate atom–atom
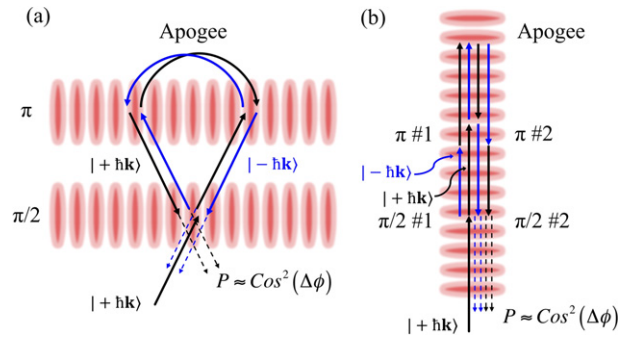
Figure 2. Example schematic of a four-pulse AI. (a) Horizontal setup. A cloud with some initial momentum is interrogated by a lower beam tuned to implement a $\pi/2$ pulse while an upper beam, where the apogee is, operates as a π pulse. The atoms begin to fall with gravity and they are recombined with another $\pi/2$ pulse when they fall through lower interrogation beam. After, the population imbalance is measured which is a direct measurement of the atomic phase. (b) Vertical setup. The same interferometer geometry, under constant gravitational acceleration.

interactions—see section 1.4.3 and [56]. After cooling, atoms are launched on a vertical parabolic trajectory into the interrogation region, where the interferometer is created in a symmetric way around the apogee using a set of two horizontal laser beam—see figure 2(a). Different interferometer sequences can be used for ELGAR; we focus our attention on the four-pulse 'butterfly' [57] configuration, whose geometry is shown in figure 2, which consists of a sequence of $\pi/2–\pi–\pi–\pi/2$ pulses separated in time by $T–2T–T$. This configuration [58], first proposed to measure gravity gradients, shows no sensitivity to DC accelerations and offers robustness against spurious phase terms. The first interferometer pulse is a beam splitter, putting the atomic ensemble into a superposition of states. The second and third pulses deflect the states, and create a folded geometry. At the location of the second beamsplitter, the trajectories overlap and the two output ports are measured. The details of the interrogation process can be found in section 1.4.2 and [56]. In brief, among the multiple techniques for the exchange of momentum between atoms and photons, the ELGAR project will focus on Bragg diffraction and Bloch oscillations [59], based on their scalability and demonstrated efficacy [60] in highly sensitive AI setups. At the conclusion of the interferometer, each atom of the ensemble is in a superposition of the output states. For detection, we measure one observable of this quantum system, the occupancy of the states. This operation is typically accomplished using a variety of destructive readout techniques, such as fluorescence and absorption [61], to obtain the probability that an atom will be found in a particular state. This probability is a function of the relative phase acquired along the paths of the interferometer, which depends upon the variation of the interrogation laser phase during the time of the interferometer, where such variations may arise from the effect of incident GWs.

Based on the horizontal interferometer geometry presented here, we now consider the sensitivity to GWs obtained from a gradiometric configuration using two spatially separated AIs, the basis of the ELGAR detector.

1.2. GW signal from an atom gradiometer

Here we present a schematic description of how the ELGAR detector is sensitive to GWs. As shown in figure 3, we consider an atom gradiometer using two free-falling AIs placed at
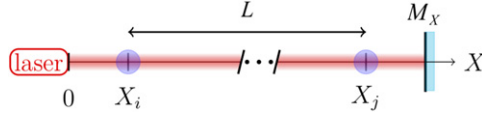
Figure 3. Gravity gradiometer schematic diagram. Two AIs placed at $X_{i,j}$ are separated by a distance L and coherently manipulated by a common laser retro-reflected by a mirror placed at position M_X. Adapted from [67].

positions $X_{i,j}$ along the x-axis and interrogated by a common laser beam which is retro-reflected by a mirror placed at position M_X. The geometry of each AI is the four-pulse ($\pi/2-\pi-\pi-\pi/2$) presented in the previous section. The interferometric signal is read out as a ground state population imbalance that depends upon the phase difference $\Delta\varphi_{\text{las}}$ between the two counter-propagating beams. Considering large momentum transfer (LMT) techniques where $2n$ photons are coherently exchanged during the interrogation process, the output phase $\Delta\phi(X_i, t)$ of the AI at position X_i and time t is:

$$\Delta\phi(X_i, t) = n \int_{-\infty}^{\infty} \Delta\varphi_{\text{las}}(X_i, \tau) g'(\tau - t) \mathrm{d}\tau + \epsilon(X_i, t), \tag{1}$$

where g' is the time derivative of the sensitivity function of the AI [62, 63] and $\epsilon(X_i, t)$ is the detection noise related to the projection of the atomic wave-function during the measurement process. Accounting for the effects of laser frequency noise $\delta\nu(\tau)$, vibration of the retro-reflecting mirror $\delta x_{M_X}(\tau)$, GW strain variation $h(\tau)$, and fluctuation of the mean trajectory of the atoms along the laser beam direction induced by the fluctuating local gravity field $\delta x_{\text{at}}(X_i, \tau)$, the last equation can be written as [40, 64]:

$$\Delta\phi(X_i, t) = \int_{-\infty}^{\infty} 2nk_l \left[\left(\frac{\delta\nu(\tau)}{\nu} + \frac{h(\tau)}{2} \right) (M_X - X_i) \right.$$
$$\left. + \left[\delta x_{M_X}(\tau) - \frac{M_X - X_i}{c} \delta x'_{M_X}(\tau) \right] - \delta x_{\text{at}}(X_i, \tau) \right] g'(\tau - t) \mathrm{d}\tau + \epsilon(X_i, t), \tag{2}$$

where $k_l = \frac{2\pi\nu}{c}$ is the wave number of the interrogation laser. It should be noted that seismic condition does not only impact movement of the retro-reflector, linked to the term $[\delta x_{M_X}(\tau) - \frac{M_X - X_i}{c} \delta x'_{M_X}(\tau)]$, but also creates frequency noise from movement of the input optics, which is included in the term $\frac{\delta\nu(\tau)}{\nu}$. By simultaneously interrogating two AIs with the same laser, one can cancel the sensitivity to position of the retro-reflecting mirror, a common-mode noise. The resulting differential phase $\psi(X_i, X_j, t)$ is [64]:

$$\psi(X_i, X_j, t) = \Delta\phi(X_i, t) - \Delta\phi(X_j, t) = \int_{-\infty}^{\infty} 2nk_l \left[\left(\frac{\delta\nu(\tau)}{\nu} + \frac{h(\tau)}{2} - \frac{\delta x'_{M_X}}{c} \right) L \right.$$
$$\left. + \delta x_{\text{at}}(X_j, \tau) - \delta x_{\text{at}}(X_i, \tau) \right] g'(\tau - t) \mathrm{d}\tau + \epsilon(X_i, t) - \epsilon(X_j, t). \tag{3}$$

With the assumption that the detection noise is spatially uncorrelated, we write the power spectral density (PSD) of the differential interferometric phase as:

$$S_\psi(\omega) = (2nk_l)^2 \left[\left(\frac{S_{\delta\nu}(\omega)}{\nu^2} + \frac{S_h(\omega)}{4} + \frac{\omega^2}{c^2} S_{\delta x_{M_X}}(\omega) \right) L^2 + S_{\text{NN}_1}(\omega) \right] |\omega G(\omega)|^2$$
$$+ 2S_\epsilon(\omega), \tag{4}$$

where S_u denotes the PSD of a given time function $u(t)$. The term $G(\omega)$ represents the Fourier transform of the sensitivity function of the interferometer to phase variations, which for the four-pulse configuration is [63]:

$$|\omega G(\omega)|^2 = 64 \, \sin^2(\omega T) \sin^4 \left(\frac{\omega T}{2} \right), \tag{5}$$

In equation (4) the term $S_{\mathrm{NN}_1}(\omega)$ is the PSD of the relative displacement of the atom test masses with respect to the interrogation laser:

$$\mathrm{NN}_1(t) = \delta x_{\mathrm{at}}(X_j, t) - \delta x_{\mathrm{at}}(X_i, t), \tag{6}$$

which is related to the difference of the local gravity field between the points X_i and X_j projected along the gradiometer direction, so-called NN, i.e. terrestrial gravity perturbations of various origins, which we treat in detail in [56]. This perturbation introduces an atomic phase variation that is indistinguishable from the signal produced by an incident GW, as shown in equation (4), and constitutes a limit for the detector that sums with other contributions.

Taking the GW term as the signal of interest in equation (4) and dividing it by the other terms, we obtain the signal to noise ratio (SNR) of the detector. Setting the limit of detection as an SNR of 1, we define the strain sensitivity of the gradiometer as the sum:

$$S_h = \frac{4S_{\delta\nu}(\omega)}{\nu^2} + \frac{4S_{\mathrm{NN}_1}(\omega)}{L^2} + \frac{4\omega^2 S_{\delta x_{M_X}}(\omega)}{c^2} + \frac{8S_\epsilon(\omega)}{(2nk_l)^2 L^2 |\omega G(\omega)|^2}. \tag{7}$$

Here, we have derived the sensitivity of an atom gradiometer to changes in space–time strain, a configuration which is the basis of the ELGAR detector. We now present the full instrument geometry which is configured to optimize the sensitivity to the different noise term listed in equation (7).

1.3. The ELGAR detector

1.3.1. ELGAR structure. In order to manage the different terms limiting the strain sensitivity of a single atom gradiometer and given in equation (7), we propose for ELGAR a detector structure shown figure 4. The distinct feature of this geometry is the use of a 2D-array of AIs, interrogated by a common laser beam in order to reduce sensitivity to gravity-gradient noise. Such a noise source is expected to be one of the main limitations of the sensitivity at low frequency of the next generation GW detectors based on optical interferometry, like the Einstein Telescope [12]. Detectors relying on single atom gradiometers will be strongly limited in their performances by GGN in a large portion of their sensitivity window, and it will be crucial to mitigate its impact. To this end, we use a sensor geometry of an optimised array to statistically average GGN [40], and bring its contribution below the target sensitivity of the instrument.

In this geometry the laser field is divided by a beam-splitter and retro-reflected by two end mirrors in order to obtain two symmetric and perpendicular arms in gradiometric configuration. Using parameters from [40], each arm of ELGAR is composed by $N = 80$ atom gradiometers of baseline $L = 16.3$ km, regularly spaced by a distance $\delta = 200$ m, leading to a total arm length of $L_\mathrm{T} = (N-1)\delta + L = 32.1$ km.

The whole detector is placed in ultra high vacuum with a residual total pressure less than $\leqslant 1 \times 10^{-9}$ mbar in order for gas collisions from the environment to play a marginal role in the operation of the individual AIs. This would make the ELGAR vacuum vessel similar in terms of size to that of existing large experiments such as VIRGO/LIGO. Such vacuum
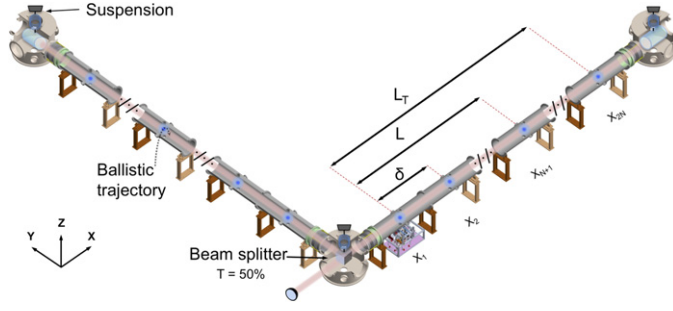
Figure 4. Schematic diagram of the proposed ELGAR infrastructure. Each arm of the detector of total length L_T is formed by N gradiometers of single baseline L. The gradiometers are spaced by a distance δ. The retro-reflection mirrors and the beam splitter are placed on suspension systems. The entire detector is inside a large steel vacuum vessel that maintains a base pressure of $\leqslant 1 \times 10^{-9}$ mbar. A vertical arm could be added at the same location or on a distributed site.

performances could be reached with a series of pumping stations distributed along the arms, containing oil-free backing pumps and large turbo-molecular pumps but also non-evaporable getters and ion pumps used after initial evacuation to reach high vacuum conditions. The individual atom sources are encased inside a magnetic shield sufficient to attenuate the Earth's magnetic field by a factor 1000 and the interrogation region is placed in a magnetic shield that covers the vacuum vessel in the few meters around each atom source; an example of such system is the magnetic shielding of the MIGA demonstrator [65].

1.3.2. ELGAR GW signal extraction and strain sensitivity. To extract the GW signal, we consider the difference between the average signals of the gradiometers of each arms:

$$H_N(t) = H_N^X(t) - H_N^Y(t) = \frac{1}{N} \sum_{i=1}^{N} \psi(X_i, X_{N+i}, t) - \psi(Y_i, Y_{N+i}, t). \tag{8}$$

Using equation (3) we obtain:

$$
\begin{aligned}
H_N(t) = \frac{1}{N} \sum_{i=1}^{N} \int_{-\infty}^{\infty} 2nk_l &\left[\left(-\frac{\delta\nu_{\mathrm{Bs}}(\tau)}{\nu} + h(\tau) - \frac{\delta x'_{M_X}}{c} + \frac{\delta x'_{M_Y}}{c} \right) L \right. \\
&\left. + \delta x_{at}(X_{N+i}, \tau) - \delta x_{at}(X_i, \tau) - \delta x_{at}(Y_{N+i}, \tau) + \delta x_{at}(Y_i, \tau) \right] g'(\tau - t)\mathrm{d}\tau \\
&+ \epsilon(X_i, t) - \epsilon(X_{N+i}, t) - \epsilon(Y_i, t) + \epsilon(Y_{N+i}, t). \tag{9}
\end{aligned}
$$

Using this differential signal cancels the contribution of common frequency fluctuations of the interrogation laser, the only differential contribution coming from horizontal movement of the beam-splitter that creates a frequency noise $\delta\nu_{\mathrm{Bs}}$ in the Y-arm of the detector:

$$\frac{\delta\nu_{\mathrm{Bs}}(\tau)}{\nu} = \frac{\delta x'_{\mathrm{Bs}_X}}{c} - \frac{\delta x'_{\mathrm{Bs}_Y}}{c}, \tag{10}$$

where δx_{Bs_X} and δx_{Bs_Y} are the variation of position of the beam-splitter along X and Y direction. Considering that the detection noise, the end mirror and the beam-splitter displacements are

uncorrelated, and supposing $S_{\delta x_{M_X}} = S_{\delta x_{M_Y}} = S_{\delta x_{Bs_X}} = S_{\delta x_{Bs_Y}}$; we can write the PSD of the average signal H_N as:

$$S_{H_N}(\omega) = (2nk_l)^2 \left[\left(S_h(\omega) + \frac{4\omega^2}{c^2} S_{\delta x_{M_X}}(\omega) \right) L^2 + S_{NN}(\omega) \right] |\omega G(\omega)|^2 + \frac{4S_\epsilon(\omega)}{N}. \quad (11)$$

In this last equation, S_{NN} is the PSD of the differential displacement introduced by the NN on the test masses of the network NN(t), defined by:

$$NN(t) = \frac{1}{N} \sum_{i=1}^{N} \left[\delta x_{at}(X_{N+i}, t) - \delta x_{at}(X_i, t) - \delta x_{at}(Y_{N+i}, t) + \delta x_{at}(Y_i, t) \right], \quad (12)$$

Following the method discussed in the previous section, we obtain the strain sensitivity of the detector exploiting the average signal as:

$$S_h(\omega) = \frac{4\omega^2}{c^2} S_{\delta x_{M_X}}(\omega) + \frac{S_{NN}(\omega)}{L^2} + \frac{4S_\epsilon(\omega)}{N(2nk_l)^2 L^2 |\omega G(\omega)|^2}. \quad (13)$$

In comparison with the result obtained for a single gradiometer, we observe that this configuration enables to mitigate the influence of the frequency noise of the interrogation laser, while preserving sensitivity to GWs with + polarization. Evenmore, considering the average signal also enables to partially mitigate the influence of gravity gradient noise exploiting the space–time correlation properties of its different sources. This process is detailed in [56]: in brief, assuming that the main sources of gravity gradient noise comes from isotropic density fluctuations of the medium surrounding the detector linked to seismic activity and atmospheric pressure variations, the averaging and correlation of the gradiometric phase from all participating gradiometers in the two arms enables to significantly reduce the unwanted signal from the gravity gradient noise [40], related to the term S_{NN} in equation (13). Indeed, in units of strain$/\sqrt{Hz}$, this technique can reduce the contribution from GGN by a factor $1/\sqrt{N}$ in comparison with the one of a single gradiometer, and can perform even better than $1/\sqrt{N}$ if the appropriate considerations are taken for optimizing the position of the gradiometers and the detector site has adequate properties. For what concerns direct effect of seismic noise, related to the term $S_{\delta x_{M_X}}$ in equation (13), this configuration has a similar sensitivity to the one of a single gradiometer. Using a dedicated low frequency seismic attenuation system for the mirrors of the detector will be necessary to reduce its effects, see further details in section 1.4.4 and [56], where we evaluate in the necessary high quality isolation and suspension system, which adopts and pushes forward key concepts devised for GW detection based on optical interferometry.

After mitigation of the different noise sources, the sensitivity of the detector is related to detection noise which is the last term in equation (13). This term is strongly related to the atomic species used in the AI as well as to the transition and techniques used for detection. The ELGAR detector can be run with different atom sources—see section 1.4.3 for a discussion on the considered atomic species. Considering the use of ^{87}Rb atoms launched onto a ballistic trajectory at a flux of 10^{12} atoms/s, an atom shot noise limited detection, a number of photon transferred during the interrogation of $2n = 1000$, and an integration time of $4T = 800$ ms, this sets a detection noise limited strain sensitivity of about $4.1 \times 10^{-21}/\sqrt{Hz}$ at 1.7 Hz for a single gradiometer of the network. Considering the detection noise of the $2N$ gradiometers is independent, the shot noise limited sensitivity of the whole detector goes as $1/\sqrt{2N}$ and improves to about $3.3 \times 10^{-22}/\sqrt{Hz}$ at 1.7 Hz.

In this section, we considered the main noise sources listed in equation (7) which are relevant for the functioning principle and geometry of the detector. Other relevant backgrounds impinging on the instrument's sensitivity are considered exhaustively in [56]. Specifically, we studied the coupling to the instrument signal of parameters associated to the atomic sources (e.g. position, velocity, temperature and momentum spread of each atomic cloud), the manipulation beams (e.g. their pointing jitter, and relative alignment), and the environment fluctuations (e.g. gravity and its gradient, the magnetic and electric field, the blackbody radiation). The impact of such background in terms of differential phase noise contribution are listed in section 2.

1.4. ELGAR technologies

A detailed description of the different technological bricks for the construction of ELGAR can be found in [56] and are summarized in the following section. We first presents different installation sites for the infrastructure in Italy and France, which are evaluated in terms of ambient noise. We then detail the realization of the matter wave beam splitters, the atom source and the suspension system required for the interrogation optics of the interferometer.

1.4.1. Detector site. Candidate sites for ELGAR must meet strict environmental requirements, as previous studies have shown for both GW detector and AI-based experiments. In considering a site, practical concerns such as feasibility of installation and local infrastructure must also be considered. Seismic noise has proven to be a major concern for AI and GW detection [66, 67]; for AI, vibrations during the launch and preparation translate into readout fluctuations and spurious atomic phase from the retro-reflection mirror. Time-varying stray magnetic fields and field gradients that create a difference in readout between gradiometers are a technical noise concern that must be addressed through shielding or active compensation; to this end, a candidate site requires mapping and monitoring of magnetic fields and field gradients. Related to seismic noise, localized gravity gradient noise is an indistinguishable technical noise for GW detection in the ELGAR observation band. This kind of noise can be separated into seismic and atmospheric components, placing importance on local geographic and climatic features of a candidate site. A site must be far from and protected against anthropogenic noise; this noise is endemic throughout the ELGAR detector's observation band. This is to say that a potential detector site needs thorough characterization as well as monitoring of the local and regional seismic, magnetic, and weather activity via various sensors. To fulfill these different properties we consider different candidate sites in France and Italy: the low noise laboratory Laboratoire Souterrain à Bas Bruit (LSBB) in Rustrel in France, and two former mine complexes in Sos Enattos and Seruci located in Sardinia. All three sites are under extensive study, with the LSBB hosting the MIGA equipment in two new specifically built 150 m galleries. The LSBB was formed after the decommission of a launch control facility for the French strategic nuclear deterrence; now a ground and underground scientific infrastructure characterized by an ultra-low noise seismic and magnetic environment, the site fosters multidisciplinary interactions and approaches to fundamental and applied research with broad scientific and industrial expertise [68]. This site is the location of the MIGA project [64], where new galleries were blasted to allow for the full equipment installation. The Sos Enattos and Seruci sites are located on Sardinia, an area of Europe with low population density, low anthropogenic noise, and ancient geological structure with seismic activity among the lowest on Earth [69]. The sites contain former mine shafts with useful infrastructure like monitoring, ventilation, and elevator equipment and they are already undergoing measurement campaigns for seismic, acoustic, and magnetic activity [69]. These sites are already under

consideration for the Einstein Telescope [12] and for the Ar40 distillation tower of the ARIS project [70].

1.4.2. Atom optics. ELGAR operates as a network of differential phasemeters [51, 64], where each device consists of two AIs in a gradiometer configuration separated by a baseline L, coherently manipulated by the same circulating light fields propagating with wavenumber k_{eff}. An incident GW modulates this baseline, leading to a differential phase shift between the two AIs. To drive such an interferometer, the atom optics typically consist of composite pulses as well as high-order Bragg/Bloch transitions. This enhances the wavenumber, $k_{\text{eff}} = 2nk_l$, corresponding to the relative momentum between the two arms of the interferometer, where k_l is the single-photon wavenumber of the driving light field. Any geometries for ELGAR share similarities in that they involve atoms in free fall, show a linear scaling of the phase shift versus the effective wavenumber, and demonstrate a frequency dependent response on the pulse separation time T. Geometries involving multiple loops lead to resonant enhancement [71] and can suppress spurious phase terms [72–75], especially when combined with a useful technique for compensating the effects of static gravity gradients through a suitable frequency change of some of the intermediate laser pulses [29, 76–78]. The atom optics in AIs imprint the phase of the applied light field onto the atomic wavefunction and can manipulate the internal state of the atom. Reaching the sensitivity target for ELGAR requires LMT, boosting k_{eff}. The three most common atom optic techniques involve utilizing stimulated Raman transitions [49], Bragg diffraction [79], Bloch oscillations [80], or a combination of the three for LMT [81–90]. In addition, single-photon processes have been proposed to combat typically high requirements on the laser frequency noise [91] and demonstrated in atom interferometry [92] including LMT [93]. Effective wave numbers equal to or in excess of $1000k_l$ by combining Bragg diffraction and Bloch oscillations appear to be feasible based on the present state-of-the-art [85]. The sensitivity garnered through this process can also be selectively enhanced by switching from a broadband mode used in the detector to a resonant detection mode [71, 94].

1.4.3. Atom source. Essential to the success of each individual interferometer is the atomic source that feeds it [95]. The source affects the sensor sensitivity and defines the susceptibility to systematic effects. The generation of large ensembles at high flux is required to obtain sufficient stability in an interrogation time as short as possible. The intrinsic noise of such a two-mode sensor, with uncorrelated input states, is characterized by the standard quantum limit (SQL) $\delta\phi_{\text{SQL}} \sim 1/\sqrt{n_{\text{meas}}N}$, where n_{meas} is the number of interferometric measurements and N is the number of atoms. To reach the target sensitivity of 1 μrad$/\sqrt{\text{Hz}}$ for a single AI at the SQL, a flux of 10^{12} atoms per second is required. AIs typically employ the Alkali isotopes of potassium (^{39}K, ^{40}K and ^{41}K), rubidium (^{85}Rb and ^{87}Rb), cesium (^{133}Cs) and lithium (^{6}Li and ^{7}Li). The Alkali elements can be addressed with multiple cooling techniques that are pathways to ultracold temperatures. ^{87}Rb is the workhorse of atom interferometry in a wide range of application and is the baseline species considered in this proposal. State-of-the-art atom optics techniques are typically tested with ^{87}Rb; of particular interest is the lowest effective temperature of a few tens of picokelvin (pK) demonstrated with ^{87}Rb [96, 97]. Cesium 133 is another promising candidate, similar to ^{87}Rb, having shown applicability to LMT experiments like those measuring the hyperfine structure constant [98]. Achieving the required ultra-cold temperatures with Cs is, however, a difficult task due to its scattering length complicating an evaporative cooling process. Alkaline-earth atoms and transition metals/lanthanoids that resemble alkaline-earth atoms like strontium (^{87}Sr and ^{88}Sr) and ytterbium (^{171}Yb) are typically used in atomic clocks for their narrow linewidth optical transitions and show significant promise for atom interferometry. These classes of atoms are immune to the quadratic Zeeman shift, setting them apart from other species. LMT single-photon transitions have been demonstrated with

these species [92, 93]. Prime candidates for an ELGAR detector based on alkaline-earth species revolve around Sr and Yb isotopes. Atomic sources for the species under consideration typically take the form of a 2D+ MOT fed either by a dispenser or an oven, which could be directly loading the trap or going through a Zeeman slowing stage. The stringent flux requirements can be relaxed by employing an atomic source that goes past the SQL—this can only be done by using non-classical input state, so entangled state. Such an entangled source can be generated via atom–light interactions like a quantum non-demolition measurement or cavity feedback or through atomic collisions [99]. The most promising results have demonstrated an 18.5 dB enhancement, what is equivalent to a 70-fold increase in the atomic flux [100, 101]. A gain of 20 dB corresponds to a factor 100 reduction in the required atomic flux and is a very active line of research worldwide.

1.4.4. Seismic isolation.　GW detectors, with laser or matter-wave interferometry, maintain the same fundamental principle of operation: the distance between two free falling inertial test masses is precisely measured with a stable laser in order to detect tiny modulations that can only be attributed to GWs. In the framework of ELGAR, the role of test masses is played by the atoms which are in free fall, and therefore naturally isolated from seismic vibrations. By comparison to optical GW detectors, using free falling test masses allows for an important reduction of the impact of seismic noise at low frequencies. The first term of equation (13) shows that seismic noise creates a spurious GW strain $S_h^{1/2}(\omega)$ with a scale factor $2\omega/c$: at 1 Hz seismic noise is filtered by a factor $\sim 2 \times 10^{-8}\,\mathrm{m}^{-1}$ whereas in a $\simeq 3$ km laser interferometer like VIRGO this factor is $\simeq 3 \times 10^{-4}\,\mathrm{m}^{-1}$. In spite of this advantage, adequate vibration isolation equipment is still required for an ELGAR detector due to the residual coupling from vibrations of the retroreflecting mirrors and the beamsplitter: to reach the target sensitivity goals of ELGAR in the 0.1–1 Hz range, the limit on the displacement noise of these elements needs to range from $5 \times 10^{-11}\,\mathrm{m\,Hz}^{-1/2}$ at 0.1 Hz to $8 \times 10^{-15}\,\mathrm{m\,Hz}^{-1/2}$ at 1 Hz. These requirements are challenging, and so constitute an active line of research for a terrestrial based AI based GW detector. A simple double suspension system [102] with a resonance frequency at 10 mHz could begin to meet ELGAR requirements, but it would require a 25 m simple pendulum—this is impractical and expensive. Due to geometric/space requirements and the observation band of interest, a new solution is needed that is not a simple upgrade of the super attenuators in optical GW detectors [103]. One example ELGAR may follow is that of AIGO [102], where they demonstrate a compact isolation and suspension system using two stages of horizontal pre-isolation and a single stage of vertical isolation. This system consists of self-damping pendulums, Euler springs [104], and Niobium ribbon suspension. Furthermore, the system employs a LaCoste linkage in vertical pre-isolation [105], while the second stage of horizontal pre-isolation is based on a Roberts linkage [106]. Such methods could possibly be further extended toward lower frequencies to meet the requirements of ELGAR, but it will require coping with the issue of losses and anelasticity [107, 108].

2. ELGAR sensitivity and data

2.1. ELGAR operating parameters and sensitivity curve

The configuration parameters of the ELGAR detector corresponding to an atom shot noise limited sensitivity of $3.3 \times 10^{-22}\,\mathrm{Hz}^{-1/2}$ at the peak frequency of 1.7 Hz are summarised in table 1. We list in table 2 the noise requirements to reach such sensitivity that we subdivided into three parts. The first line corresponds to the atom shot noise contribution that is, by

Table 1. Parameters of the ELGAR detector to reach a strain sensitivity of $3.3 \times 10^{-22} \, \mathrm{Hz}^{-1/2}$ at the peak frequency of 1.7 Hz limited by atom shot noise.

Atomic source	
Species	$^{87}\mathrm{Rb}$
Loading source	2D + MOT
Equivalent atomic flux[a]	$1 \times 10^{12} \, \mathrm{s}^{-1}$
Ensemble type	Ultracold source
Expansion velocity ($T_{\mathrm{eff}} \approx 100 \, \mathrm{pK}$)	$100 \, \mu\mathrm{m \, s}^{-1}$
Vertical launching velocity	$4 \, \mathrm{m \, s}^{-1}$
Cloud size[b]	16 mm

Detector	

Single gradiometer	
Configuration	Double loop, four pulses
Interrogation time	$4T = 800 \, \mathrm{ms}$
Atom optics	Sequential Bragg
Momentum transfer	$2n = 1000 \, \hbar k$
Baseline	$L = 16.3 \, \mathrm{km}$
Peak strain sensitivity (at 1.7 Hz)	$4.1 \times 10^{-21} \, \mathrm{Hz}^{-1/2}$

Full detector	
Number of gradiometers per arm	$N = 80$
Gradiometer separation	$\delta = 200 \, \mathrm{m}$
Total baseline	$L_{\mathrm{T}} = 32.1 \, \mathrm{km}$
Peak strain sensitivity (at 1.7 Hz)	$3.3 \times 10^{-22} \, \mathrm{Hz}^{-1/2}$

[a] $1 \times 10^{10} \, \mathrm{s}^{-1}$ + 20 dB squeezing (in variance) or $1 \times 10^{12} \, \mathrm{s}^{-1}$.
[b] Assuming 10 interleaved interferometers, 1×10^{9} atoms and 20 dB squeezing.

design, the dominant noise contribution. The second part (lines 2–7) accounts for the degree of controllability of the atomic motion and of the atom optics, for their mutual couplings, and for the couplings to the environment. The third part (lines 8–10) covers the influence of static electric and magnetic fields to the atoms.

The details of the calculation of the requirements of table 2 are given in [56]. We present here the list of the different noise contributions for self-consistency. Equation (13) gives the link between the strain sensitivity of the whole detector and the phase noise level of a single AI forming the array as:

$$\sqrt{S_h(\omega)} = \frac{1}{\sqrt{N}} \times \frac{1}{2nk_lL|\omega G(\omega)|} \times 2\sqrt{S_\epsilon(\omega)}, \tag{14}$$

The target floor sensitivity level of $3.3 \times 10^{-22}/\sqrt{\mathrm{Hz}}$ for the array of $2N$ uncorrelated gradiometers corresponds to the strain sensitivity for a single gradiometer of $4.1 \times 10^{-21}/\sqrt{\mathrm{Hz}}$ which is reached at the peak frequency of 1.7 Hz. This, in turn, sets the differential atom phase sensitivity limit of $\sqrt{2S_\epsilon^{\mathrm{lim}}} = \sqrt{2} \times 10^{-6} \, \mathrm{rad}/\sqrt{\mathrm{Hz}}$, with $\sqrt{S_\epsilon^{\mathrm{lim}}}$ being the atom shot noise

Table 2. Noise requirements for the ELGAR detector [56] to reach the designed strain sensitivity.

Noise source	Constraint
1. Phase noise from atom shot noise[a]	$1\ \mu\text{rad Hz}^{-1/2}$
2. Velocity noise (coupled to static rotation)[b]	$50\ \text{nm s}^{-1}\ \text{Hz}^{-1/2}$
3. Static relative beam alignment[c]	0.32 nrad
4. Compensation of static gravity gradient[d]	1%
5. Relative beam angle jitter (coupled to imperfect velocity)	$4\ \text{prad Hz}^{-1/2}$
6. Laser beam pointing jitter (coupled to static gravity difference)	$0.3\ \text{prad Hz}^{-1/2}$
7. Wavefront curvature coupled to velocity noise[e]	$0.8\ \text{nm s}^{-1}\ \text{Hz}^{-1/2}$
Acceleration noise from:	
8. Magnetic field[f]	$0.1\ \text{nT Hz}^{-1/2}$
9. Blackbody radiation[g]	$2\ \text{mK Hz}^{-1/2}$
10. DC Stark shift[h]	$0.2\ \text{V m}^{-1}\ \text{Hz}^{-1/2}$

[a]Based on the equivalent atomic flux in table 1.
[b]Assuming a rotation rate of 73 μrad s^{-1} (Earth rotation rate).
[c]Assuming an initial velocity noise of the atoms of 50 nm s^{-1} Hz$^{-1/2}$.
[d]Gravity gradient $\Gamma \approx 1.5 \times 10^{-6}$ s^{-2} and assuming a source velocity noise of 50 nm s^{-1} Hz$^{-1/2}$.
[e]The laser beam radius of curvature is 25 km (Gaussian beam waist of 50 mm).
[f]Assuming a magnetic field gradient of 1 nT m^{-1}.
[g]Assuming a temperature gradient of 0.1 K m^{-1}.
[h]Assuming an electric field gradient of 0.1 V m^{-2}.

limited phase sensitivity of a single interferometer. In deriving the noise requirements, we restrict the analysis to the case of a single interferometer and assume uncorrelated phase noise between the interferometers forming the array. We set a conservative requirement for each of the spurious phase noise contributions to not exceed the level of 0.1 μrad/$\sqrt{\text{Hz}}$ at 1.7 Hz for a single AI. The main noise sources evaluated in reference [56] are:

- Couplings of Earth rotation (table 2, line 2), gravity gradients (line 4), beam misalignment (line 3) and beam pointing jitter (line 5) to the initial position and velocity noise of the atom source, and coupling of beam pointing jitter to gravitational acceleration differences along the detector baseline (line 6);
- Magnetic fields, electric fields, blackbody radiation (lines 8, 9, 10)
- Impact of differential wavefront distortions (line 7);
- Scattered light and diffraction phase shifts (not in the table);
- Effect of inter-atomic interactions (not in the table).

The atom shot noise limited sensitivity curve of ELGAR, calculated with the parameters of table 1, is illustrated in figure 5. For what concerns Seismic and NNs, the strategies adopted to mitigate them below the atom shot noise are discussed in [56]. All the other noise sources are then kept below atom shot noise according to the parameters of table 2. On the ELGAR sensitivity curve, the interrogation time T sets the corner frequency of maximum strain sensitivity at 1.7 Hz. The resonance peaks correspond to the windowing effect of the AI captured by the transfer function $|\omega G(\omega)|$ [63]. As discussed in section 1.4.2, ELGAR can accommodate different geometries including single- and folded triple-loop to improve the sensitivity at lower frequency or better suppression of the spurious phase terms. As shown in [56], by varying slightly the interrogation time T, ELGAR can operate in broadband mode to detect
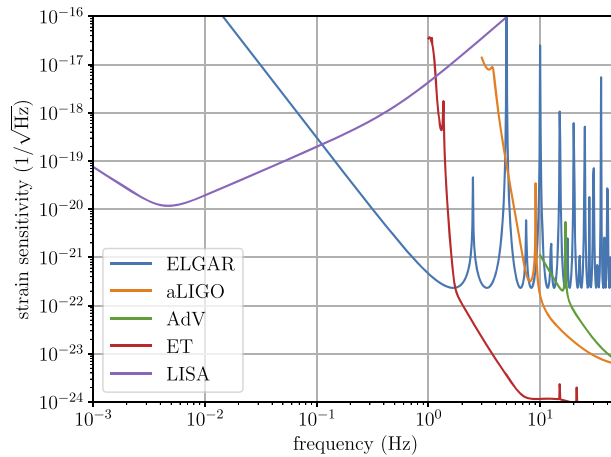
Figure 5. Strain sensitivities for different GW detectors, including ELGAR (atom shot noise limit), aLIGO, ET and LISA; they cover the frequency range from 10 mHz to 10 Hz.

unknown GW signals and later switch to resonance mode to enhance the signals at specific frequencies.

2.2. ELGAR within the global framework of GW detectors

ELGAR will complement the existing optical gravitational-wave instruments such as Advanced LIGO (aLIGO) and Advanced Virgo (AdV), and the future detectors such as Einstein Telescope (ET) and LISA, by covering a frequency band gap between the sensitivity curves of ground-based and space detectors. The strain sensitivities for different detectors including ELGAR, aLIGO, AdV, ET and LISA are illustrated in figure 5. As stated before, the resonance peaks in the ELGAR sensitivity curve correspond to the windowing effect of the AI and can be overcome by operating the antenna in a broadband mode [56]. The ground-based detectors such as aLIGO or AdV are limited by seismic and thermal noises for frequency below 10 Hz. The space-based detectors including LISA can operate at a much lower frequency band from 0.1 Hz to mHz thanks to the large absence of Newtonian gravitational fluctuations in space. ELGAR therefore offers a unique opportunity to explore GWs in the deciHertz band where an ambitious science program can be carried out. The new possibility offered by ELGAR for astrophysics, gravity and fundamental physics will be detailed in section 3.

2.3. Data management for the GW and geophysical, atmospheric and environmental monitoring communities

The ELGAR detector will generate two kinds of data: the atom interferometry strain sensor output, providing the time series $h(t)$ of the GW induced strain, and a large number of ancillary data from a whole range of environmental sensors. ELGAR will produce strain data at much higher spatial resolution in a frequency band substantially lower than those of the existing detectors. This offers the unique opportunity to compare this gravitational data with other local measurements. Inversely the GW final strain data will benefit from the combination of existing and new data, to disentangle the effect of GW from that of classical NN. The exploration of

the parameter space of gravitational-wave sources is a large-scale effort that involves many research groups and relies on interaction between gravitational-wave source modeling groups and the gravitational-wave data-analysis community.

State-of-the-art methods seek to address these challenges by considering data encoded in large-scale matrices and employ tools like principal component analyses (PCA), singular value decomposition and non-negative matrix factorization. Despite their capabilities, a number of inherent limitations characterize these approaches, including the inability to encode high-dimensional observations or data from multiple sources/modalities. Furthermore, these approaches are data-agnostic, which limits their potential for the specific setting. Within ELGAR, novel mathematical frameworks will be exploited and developed, by modeling observation using high-dimensional data structures known as multi-way tensors, investigating approaches like robust tensor PCA, and low-rank tensor recovery. Furthermore, available observations could be exploited into a supervised machine learning algorithm in order to introduce methods like deep tensor neural networks for the optimal representation of measurements.

Specifically, the envisioned data management framework will offer a number of novel capabilities in terms of multi-modal high-dimensional data observation quality enhancement. First, it will support the separation of the contribution of different noise sources from the observations by identifying the essential statistical characteristics, both in the time as well as the frequency domain for each signal category. In addition, it will offer the ability to perform joint analysis of multiple time series of *in situ* measurements from deployed sensing networks. By developing a unified framework, a variety of signals from disparate origins, represented in different forms (e.g., time-series and imagery) will be (jointly) processed in order to characterize their spatio-temporal evolution, and thereby facilitate the calculation of the geophysical computational models. Last, it will act as the core framework for the imputation of missing measurement from different spatial locations and temporal instances, recovering lost measurements due to sensor and/or storage failures, exploiting properties like model sparsity and low-rank characteristics.

In addition to the enhancement of the quality of observations, the developed framework will also support the clustering and detection of anomalies through cutting-edge signal modeling and learning. This objective will be achieved by autonomously generating the nominal data space, considering key operational characteristics parameters of each sensor category (e.g., nominal range of values, sensitivity, accuracy, and drift). Based on this information, the sensing uncertainties will be automatically estimated, exploiting their representation in lower-dimensional spaces, which will both automatically update the nominal operational bounds, as well as indicate when specific regions of data exceed these bounds, due to the existence of short (e.g. outlier) or longer (e.g., hardware) failure of the sensing infrastructure. To accommodate the expected increased volume of the data collected and the expectation of providing reduced, yet equivalently informational observations, we will employ cutting-edge machine learning algorithms, focusing on deep learning architectures, for inferring the optimal anomaly detection policies in a completely unsupervised way [109]. Furthermore, the state-of-the-art could be extended by simultaneously considering observations from multiple modalities/sources and time-instances [110] into the anomaly detection policies.

For supporting the above goals, the data storage and access needs of ELGAR will be studied in order to propose the proper storage and computing infrastructure to meet them. In order to estimate infrastructure requirements, the landscape of the ELGAR's data will be analyzed in four dimensions: (a) their size, (b) their access patterns, (c) their processing needs, and (d) the robustness of the proposed approach(es). Then the serving model of the data will be analyzed along with the different computing infrastructure options that can better serve the data

requirements. User-friendly and customizable ways to access the data and formulate information needs will also be consider, mainly based on the ontology-based data access paradigm and exploratory approaches, allowing the integration and interoperation among different scientists and data repositories.

3. Astronomy and physics with ELGAR

The first few years of GW astronomy, made possible by the large optical instruments LIGO [8] and Virgo [9], have significantly altered our knowledge and expectations about GW sources. The first detection, the GW150914 event [1], consisting of a pair of $36M_\odot + 29M_\odot$ BHs, merging into a final $62M_\odot$ BH, and the subsequent multiple GW observations have demonstrated that binary BH (BBH) signals are by a factor $\mathcal{O}(10)$ the dominant component of the observed mass spectrum [111] of GW sources. Earlier, BNS coalescences were considered the most likely source of GWs: the period evolution in systems like the Hulse–Taylor binary pulsar (PSR B1913 + 16) with the predicted loss of orbital energy had provided indirect confirmation of the emission mechanism [112] (see also [113]), and the observational evidence, by way of the pulsar phenomenon, of several BNS systems in our Galaxy resulted in a credible estimate for an event rate [114, 115]. These predictions were actually confirmed when in the summer of 2017 LIGO and Virgo observed the first BNS event [116], yet BBH events remain prevalent. The abundance of BBH events is *a posteriori* understandable: the GW signal amplitude scales roughly as $h \propto M^{5/3}$, hence a $\sim 30 + 30M_\odot$ BBH system is roughly detectable $\mathcal{O}(10)$ farther away than a $10 + 10M_\odot$ BBH system, previously taken as a benchmark. The observed volume scales approximately with the cube of the maximum observable distance, which explains the observed $\mathcal{O}(10^3)$ rate enhancement over the benchmark. We remark that even a single BNS observation, GW170817 [116, 117], has had an immense scientific value, also thanks to the association with a gamma-ray burst [117], confirming a long standing hypothesis about the gamma-ray burst (GRB) origin [118]. From the LIGO-Virgo observations during the two first observing runs [111], O1 and O2, the merger rate estimated for BNSs is 110–3840 Gpc^{-3} yr^{-1} (90% confidence intervals), and for BBHs is 9.7–101 Gpc^{-3} yr^{-1}. Given that there are no established detections for BH–NS mergers, only upper limits can be established and all of them (also 90% confidence intervals) are below 610 Gpc^{-3} yr^{-1}.

The observations of LIGO and Virgo belong to the high-frequency band, between $1–10^4$ Hz, although current sensitivities do not go below 20 Hz. There are two other bands where there is significant progress toward the direct direction of GWs: (i) the low frequency band, between $10^{-5}–1$ Hz, not accessible from ground due to seismic and gravity-gradient noises, where space-based detectors can operate. (ii) The very-low frequency band, between $10^{-9}–10^{-6}$ Hz, the realm of pulsar timing arrays (PTAs). The low-frequency band has already a space mission selected (on June 2017), the Laser Interferometer Space Antenna (LISA) [119], the L3 mission of the European Space Agency with a launch date expected in 2034. LISA will consist in a triangular constellation of three spacecrafts exchanging laser beams and 2.5 million km of arm-length trailing the Earth on a heliocentric orbit. The required sensitivity is attained by suppressing the laser frequency noise below the secondary noises by a combination of laser frequency locking and noise cancellation via time-delay interferometry. The LISA Pathfinder mission [120–122] has demonstrated, between December 3, 2015 and June 20, 2017, the main technology for LISA. LISA has a very wide science case as described in the white paper *The Gravitational Universe* [123]. On the other hand, in the very-low frequency band several consortia of radiotelescopes measure, over long time spans, the time of arrival of radio-pulses emitted by well-chosen sets of (millisecond) pulsars. By correlating

the measurements from the different pulsars, deviations in the times of arrival of the radio-pulses due to passing GWs are sought. There are three PTA collaborations: the European PTA (EPTA [124]), the North American Nanohertz Observatory for GWs (NANOGrav [125]), and the Parkes PTA (PPTA [126]). They form the International PTA (IPTA [127]) with the aim of enhancing the sensitivity by combining the data of the individual PTAs. The sensitivity of these PTAs is already inside the predicted discovery space for GW backgrounds produced by the emission of inspiraling supermassive BH binaries, with masses between 10^8–$10^{10}M_\odot$.

The decihertz GW band, between 0.1–10 Hz, where we do not have any current detector (not even approved for construction), is very rich in GW sources, which is reflected in the fact that it is the bridge between two distinctive GW bands in terms of sources, the high-frequency band, where second-generation ground based detectors have already observed a number of sources [111], and the low-frequency band, where LISA [119] will operate. The main sources for this band, as it happens with the high- and low-frequency bands, are coalescing compact binaries. The components of these binaries can be diverse: mainly white dwarfs, NSs and BHs. Among the BHs we have to differentiate them according to mass (stellar-mass BHs and intermediate-mass BHs) and origin (stellar origin, globular clusters, early Universe). It is also important to understand to which stages of BBH coalescence (inspiral, merger and ringdown) ELGAR is sensitive. In principle, ELGAR should detect: (i) the merger (and ringdown) of intermediate mass BBHs (with masses in the range 10^2 to $10^4 M_\odot$). (ii) The inspiral phase of stellar-mass binaries, like BBH coalescence; BNS coalescence; neutron star-BH coalescences; even binaries containing white dwarfs. (iii) Stochastic gravitational-wave backgrounds for ELGAR. We have to distinguish backgrounds due to the emission of many compact binary inspirals from those produced during the early-universe by means of high-energy processes.

3.1. Extending the BBH spectrum

The large number of BBHs already detected in the scientific runs of the LIGO and Virgo detectors (from O1 to the current O3 runs) motivates a considerable effort to better understand the origin of these systems, whether they result from the common evolution of pairs of massive stars, or form through capture mechanism in dense stellar environments [128]. To fully answer these questions, we want to characterise and extend the mass spectrum of these systems: are BBH pairs like GW150914 the most massive we should expect? Are there more massive systems to be detected, that we cannot just see yet? And it is important to measure accurately parameters like spin magnitudes and directions, which carry information about the past evolution of the system.

To address these questions meaningfully, it is necessary to enlarge the window of observation toward lower frequencies, since the maximum frequency of the GWs emitted roughly scales as M^{-1}; an event 30 times more massive than GW150914 would be confined at frequencies below ~ 10 Hz, where LIGO and Virgo are essentially blind because of seismic and suspension thermal noise. In the long term, the ground-based Einstein Telescope (ET) [12] will push the lower frequency limit down to ~ 3 Hz, thus considerably widening the range of detectable masses [129], whereas the space based LISA detector [119] will open up the mHz to Hz range to observation, making possible to detect very massive systems, and extreme events like the infall of matter into supermassive BHs.

However, we can see in figure 6 that a gap will remain which could prevent, for instance, to directly observe the merger phase of the so-called intermediate mass BHs (IMBH), systems including BHs of $\mathcal{O}(10^3 M_\odot)$. Filling this gap is one of the purposes of an AI designed for the
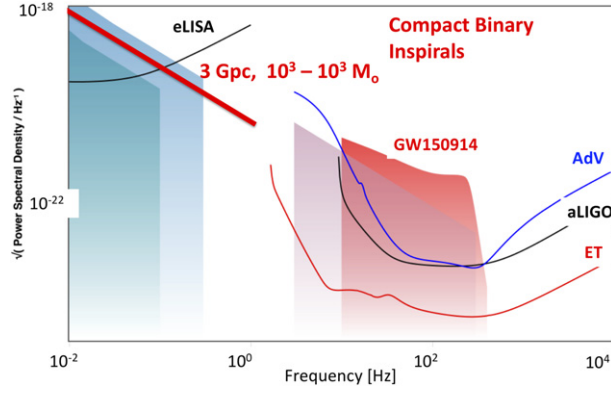
Figure 6. Design sensitivity of the second-generation ground-based detectors LIGO and Virgo, the future third-generation ground-based detector ET, and of the future space-based detector LISA, along with the trace of the BBH event GW150914, of an hypothetical IMBH event at 3 Gpc, and spectra of BNS events. Figure obtained using the GWplotter tool [130].

detection of GWs; evidence for such systems could shed light on the possible existence of a ladder of BH masses, from stellar mass to supermassive ones. An absence of evidence could indicate that entirely different formation mechanisms are at play in different mass ranges.

We can predict the waveforms emitted by massive BBHs; considering that the only relevant physical parameters are the Newton constant G_N and the speed of light c, from dimensional analysis only we have that

$$h(t, d, M_1, M_2, \mathbf{S}_1, \mathbf{S}_2) = h\left(\frac{t}{G_N \mu c^{-3}}, \frac{d}{G_N \mu c^{-2}}, \frac{M_1}{\mu}, \frac{M_2}{\mu}, \frac{\mathbf{S}_1}{G_N \mu^2 c^{-1}}, \frac{\mathbf{S}_2}{G_N \mu^2 c^{-1}}\right), \quad (15)$$

where $\mathbf{S}_{1,2}, M_{1,2}$ are the BHs spins and masses, and μ is an arbitrary mass scale. In a system (say) λ times more massive than a reference one (could be GW150914 for instance), noticing that the waveform is independent of μ, the equivalence holds

$$h\left(t, d, \lambda M_1, \lambda M_2, \lambda^2 \mathbf{S}_1, \lambda^2 \mathbf{S}_2\right) = h\left(\frac{t}{\lambda}, \frac{d}{\lambda}, M_1, M_2, \mathbf{S}_1, \mathbf{S}_2\right). \quad (16)$$

In the frequency domain

$$\hat{h}(f, d, \lambda M_1, \lambda M_2) \equiv \int_{-\infty}^{+\infty} h(\frac{t}{\lambda}, \frac{d}{\lambda}, M_1, M_2) e^{-2\pi i f t} \, dt$$

$$= \lambda \int_{-\infty}^{+\infty} h(\tau, \frac{d}{\lambda}, M_1, M_2) e^{-2\pi i \lambda f \tau} d\tau = \lambda^2 \hat{h}(\lambda f, d, M_1, M_2), \quad (17)$$

where in the last equation we have exploited the $\frac{1}{d}$ dependency of the waveform on distance. Hence the frequency evolution $f_l \to f_u$ for a system with masses $\lambda M_{1,2}$ is mapped onto the evolution $\lambda f_l \to \lambda f_u$ of a system with masses $M_{1,2}$ at the same distance, including a λ^2 factor on amplitude and λ scaling in the frequency. It follows a scaling by $\lambda^{3/2}$ of the SNR:

$$\text{SNR} \equiv 2\sqrt{\int_{f_l}^{f_u} \frac{\left|\hat{h}(f, d, \lambda M_1, \lambda M_2)\right|^2}{S_n(f)} df} = 2\lambda^{3/2} \sqrt{\int_{\lambda f_l}^{\lambda f_u} \frac{\left|\hat{h}(\nu, d, M_1, M_2)\right|^2}{S_n(\nu/\lambda)} d\nu}. \quad (18)$$

For instance, a $10^3 + 10^3 M_\odot$ BBH ($\lambda \simeq 30$ with respect to GW150914), located at 3 Gpc could be observed in the band 1–10 Hz with SNR $\simeq 5$ using a detector having a noise floor $\mathcal{O}(10^{-21}$ Hz$^{-1/2})$; even though this noise floor is 100 times worse than Advanced LIGO or Virgo, the longer duration in band of the signal would allow to accumulate a comparable SNR.

3.2. Binaries of intermediate-mass BHs

The size of a massive BH (MBH) in comparison with its host Galaxy is tiny. For instance, for an MBH with a mass of $10^6 M_\odot$ the difference spans over ten orders of magnitude. In spite of this, there is a link between the properties of the host Galaxy and the MBH. The mass of the MBH and the velocity dispersion σ of the spheroidal component is one of the best examples [131]. However, the low end of this *mass-sigma* correlation is uncertain because we lack data. By extending this correlation to smaller systems, we expect that dense stellar systems such as clusters harbor intermediate-mass BHs, IMBHs, i.e. BHs with masses 10^2–$10^4 M_\odot$ (see [132] for a review).

For two IMBHs to form a binary emitting GWs, there are two different possibilities. First, (i) two host clusters born in a *cluster of clusters*, as those which we observe in the Antennæ Galaxy (see introduction of [133]), can be gravitationally bound, and doomed to merge with each other. In this process, the IMBHs sink to the center of the system due to dynamical friction first, to form a BBH, and later that binary shrinks its semi-major axis due to interactions with stars. After each of such interactions the star can take away a bit of the energy of the BBH. If there are enough stars to interact with, the BBH evolves and eventually enters the GW-dominated regime. This means that the main driving mechanism in the evolution of the BBH are GWs, so that the orbit circularizes. This process has been described in the works of [133–135]. A space-based observatory such as LISA should detect these systems with an event rate of 4–5 yr^{-1}. Another possibility for a BBH to form is (ii) via the runaway formation of two very massive stars in a single cluster with a binary fraction of 10%, as described in [136]. In [137] it is estimated that LISA and Advanced LIGO should detect tens of them, but this depends on the distribution of the masses of the host cluster and also their central densities.

In [139] it is shown that a BBH can spend a significant amount of its evolution before the merger in the decihertz regime. In figure 7 we show two BBHs spending a significant amount of their evolution before the merger in the ELGAR regime. This means that these systems are perfect targets for ELGAR. A joint detection of these BBHs with ELGAR and the early inspiral with LISA would help to obtain enhanced measurements of the parameters and also to potentially break degeneracies. We can see on the right panel that the system merges out of the LISA window, and spends 8 min in the ELGAR sensitivity window and merges at about 1 Hz. This means that if an observatory such as LISA is operative at the same time as ELGAR, it could issue a warning years in advance with a precision of seconds.

3.3. Intermediate-mass ratio inspirals

Compact objects such as stellar-mass BHs, neutron stars or white dwarfs can form a binary with an MBH and contrary to extended stars, approach closer distances without suffering significant tidal stresses. In the process the binary system emits gravitational radiation as orbital energy is lost. Such radiation provides us with detailed information about the binary and allows us to test gravity in the strong regime. Due to the mass ratio, we talk about extreme-mass ratio inspirals because $q \gtrsim 10^4 : 1$ (EMRI, see [140, 141]). Such EMRIs are one of the main objectives of LISA [119] and form in galactic nuclei.
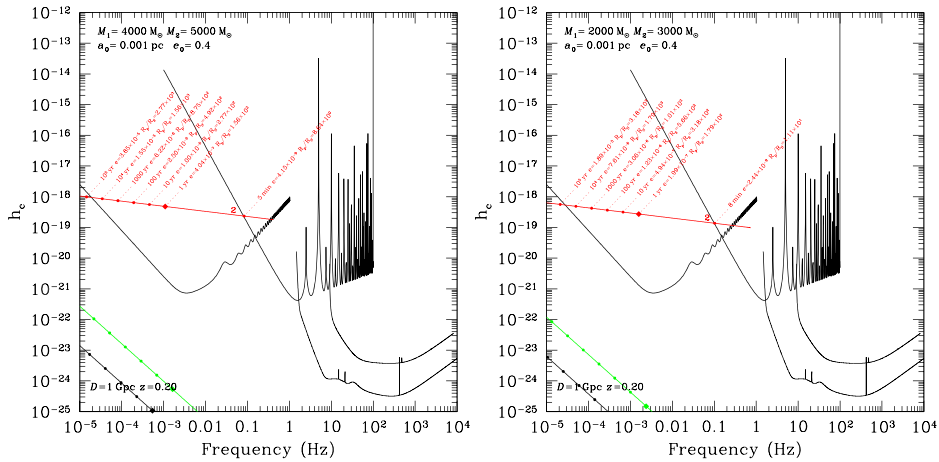
Figure 7. *Left panel*: characteristic amplitude h_c as a function of frequency for a BBH of masses $4000M_\odot$ and $5000M_\odot$. We show the initial dynamical parameters on the two left corners. The BBH initially has an eccentricity of $e_0 = 0.4$, an initial semi-major axis of $a_0 = 10^{-3}$ pc and are is located at a distance of $D = 1$ Gpc. We show the sensitivity curve for ELGAR starting at 10^{-3} Hz and $h_c \sim 10^{-14}$. We also show the curve for LISA starting at the lowest frequency, the ET starting at 1 Hz and LIGO, at 10 Hz. We display the first harmonics of the GW in the approximation of [138] and show different moments in the evolution with circles on the top of the second one. The last diamond corresponds to one year before the merger. At each of these, we additionally give the eccentricity and the periapsis distance normalised to the Schwarzschild radius. The source enters the ELGAR regime 5 min before merger. *Right panel*: same as the left panel but for slightly different masses, and 8 min before merger.

Smaller mass ratios, of $q \sim 10^2 - 10^4 : 1$ correspond to *intermediate-mass ratio inspirals* (IMRIs, see e.g. [142–144]), and are optimal sources of ELGAR. IMRIs form in smaller systems, in globular clusters, with typically very high eccentricities, via two-body relaxation or the braking mechanism, i.e. the parabolic formation of a binary, as described in [145–151]). The work of [152] is the first numerical simulation which shows the formation and evolution of an IMRI in a globular cluster. The authors observe a binary of a stellar-mass BH of mass $26M_\odot$ forming with the central IMBH, of mass $M_{BH} = 500M_\odot$ with an initial semi-major axis of $a \sim 10^{-5}$ pc and an eccentricity of $e = 0.999$, which fits in the parabolic capture mechanism of [146]. Due to the relativistic recoil [153–155], the merged system leaves the whole cluster. After this initial paper, other independent groups have found similar results, such as [156, 157]. In particular, the simulations of [158] are basically a reproduction of the set-up of [152] but with a different numerical scheme which however remarkably leads to a very similar result.

Ground-based detectors such as the proposed ET [12, 159] (with SNRs of up to ~ 2000, and are of typically a few hundred and of tens for masses up to $2000M_\odot$) but also LIGO and Virgo, can detect the final stages in the evolution of IMRIs (with SNRs of a few tens) and, depending on the eccentricity, jointly with LISA (with SNRs of a few to tens), as shown in [160]. Due to the range of frequencies that these sources have, a decihertz observatory such as ELGAR will have an important impact. In figure 8 we show the characteristic amplitude in function of the frequency of an IMRI, as well as a few different moments in the evolution.

It has also been shown in the work of [160] that by adding a decihertz observatory such as ELGAR, we can impose better constraints on the system's parameters. LISA and, later,
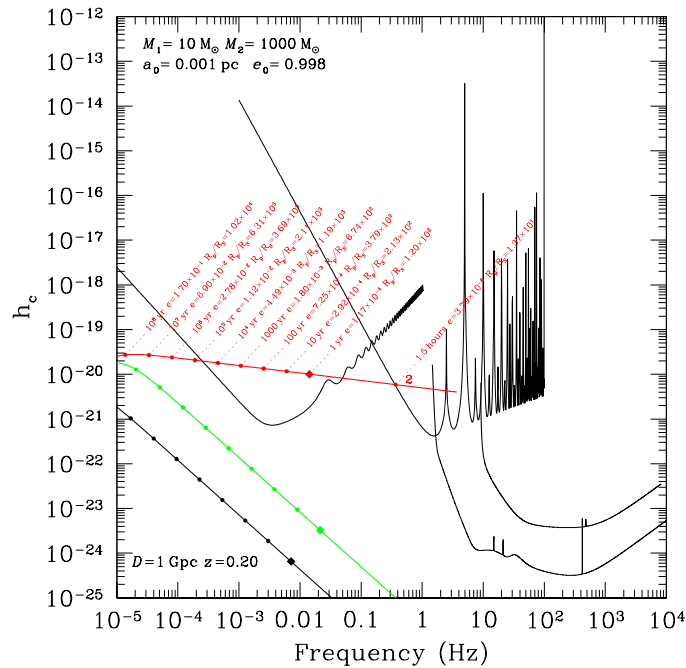
Figure 8. Same as figure 7 but for an IMRI of masses $1000M_\odot$ and $10M_\odot$. The initial eccentricity is of $e_0 = 0.998$, as we expect from these systems (see [140, 160]), and an initial semi-major axis of $a_0 = 10^{-3}$pc. The IMRI spends 1.5 h in the ELGAR regime. LISA can forewarn ELGAR years in advance and with at least seconds of precision about the time when the source enters in its domain and provide detailed information about all dynamical parameters of the system.

ELGAR can measure the inspiral and hence derive parameters such as e.g. the chirp mass. At more advanced stages in the evolution, LIGO/Virgo can detect the merger and ringdown, which allows us to derive the final mass and spin. Due to this combined detection, and contrary to an individual one, one could break various degeneracies and obtain enhanced measurements of the parameters.

3.4. Stellar-mass binaries

The LIGO and Virgo observatories cannot currently discern the formation channel of stellar-mass BBHs. In [161] it is shown that BBHs formed either dynamically or in the field via stellar evolution share identical properties, i.e. masses larger than the nominal $10M_\odot$, a mass ratio ($q \equiv M_2/M_1$) of about 1, low spin, and nearly circular orbits.

A compound detection of these detectors with LISA could allow us to to study different moments in the evolution of BBHs on their way to coalescence [119]. LISA can detect BBHs when the BHs are still 10^2–10^3 Schwarzschild radii apart, years to weeks before they enter the LIGO/Virgo band. At such separations, the orbital eccentricity in principle bears the imprint of the formation channel because (i) BBHs in dense stellar systems form on systematically more eccentric orbits and (ii) the GW radiation at this stage is too weak to circularize the orbits. Therefore, *a priori* detecting circular binaries with LISA typically would imply a formation in the field, while a detection of LISA of eccentric ones should have formed dynamically.
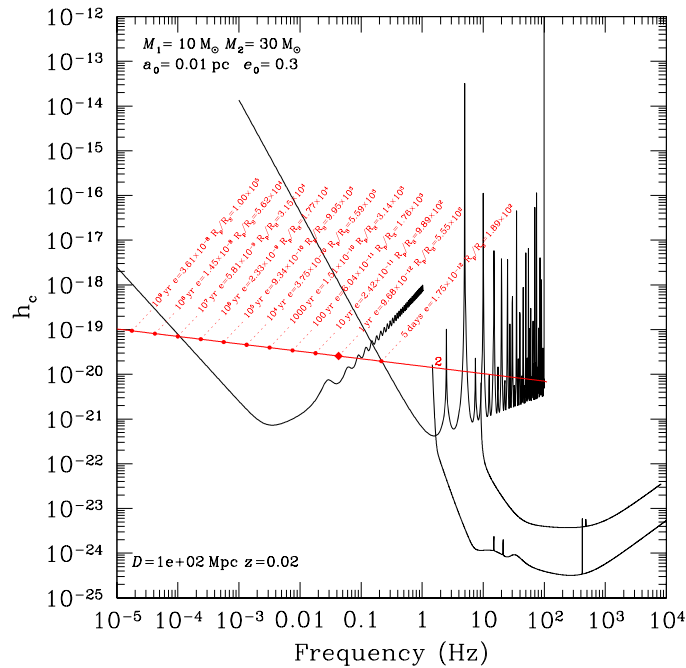
Figure 9. Same as figure 7 but for a BBH of masses $10M_\odot$ and $30M_\odot$. The system enters the ELGAR sensitivity curve five days before merger, and starting at about 0.3 Hz, crosses most of it in frequency.

Nevertheless BBHs formed dynamically stand a big chance of eluding the LISA band, as shown in [162]. Indeed, in their work the authors show that only a very small subset of the detections would lead to a joint detection with LISA and LIGO/Virgo. This means that, even if we successfully detect BBHs with LISA and LIGO/Virgo, we still will not be able to disentangle the nature of their formation. This is a consequence of LISA not being able to detect very eccentric BBHs, as shown in the work of [162], in particular their figure 1. In figure 9 we show a BBHs with an initial low eccentricity. A decihertz detector such as ELGAR would contribute to recover the information about the formation process of the binary.

3.5. Horizon reach of ELGAR for compact binary coalescence

Ground-based detectors are currently sensitive to BBH coalescence at cosmological distance distances where cosmological effects become relevant ($z \sim 2$). A measure of the capabilities of a given detector is the distance reach it has to compact binary coalescence (CBC) events. Here we show the horizon distance at which ELGAR can detect CBC events, for a given SNR threshold, in terms of the total mass of the system (as measured in the source frame). The horizon distance is the farthest luminosity distance at which a given source can be seen. That is, we are assuming optimal sky orientation and localization. For the estimation of the ELGAR horizon distance we adopt the ELGAR sensitivity shown in figure 5. In order to make this computations we have used two different GW inspiral distance calculator tools [163, 164] (see [165] for details), which we have adapted to the needs of this paper. In this way, by comparing the results from the two libraries we make sure that the answers we obtain are correct. These two libraries use in turn the LIGO Algorithm Library (LAL) [166]. To make the calculations
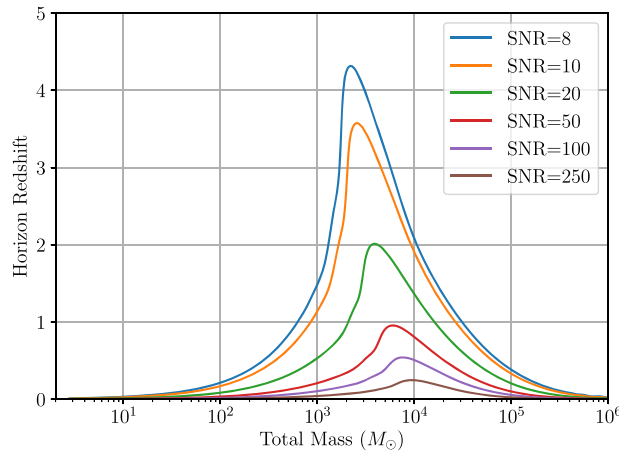
Figure 10. The plot shows the horizon redshift (in linear scale) for ELGAR detections of CBC events in terms of the total mass in the source frame (expressed in units of the Sun mass) for six different SNR detection thresholds (5, 8, 10, 20, 50, and 100).

we need to use gravitational waveforms for the CBC events. The ones we have used for the inspiral-merger-ringdown (IMR) belong to the IMR-PhenomD waveforms introduced in [167], assuming no spins. For the cosmology we have used the cosmological parameters quoted by the 2015 Planck Collaboration paper [168].

In figure 10 we show the horizon redshift in terms of the total mass (as measured in the source frame and in units of the Sun mass) for different SNRs (from 8 to 250). As we can see, assuming the detection threshold is set at SNR = 8, we can detect BBH coalescence beyond redshift $z = 4$. In figure 11 we show an equivalent plot, in the sense that we show the horizon luminosity distance instead of the horizon redshift for ELGAR, where it is shown that ELGAR can reach distances beyond 10 Gpc. Both plots show that ELGAR is most sensitive to coalescing binary systems with a total mass in the range 10^3–$10^4 M_\odot$.

3.6. Stochastic backgrounds of GWs

The incoherent sum of numerous unresolved GW signals results in a stochastic background of GWs [169, 170]. We can distinguish two types of stochastic GW backgrounds: (i) originated by high-energy processes in the early Universe: from the inflationary epoch to different phase transitions; spacetime defects of cosmological scales such as cosmic strings, etc. The energy scale of the processes associated to these physical processes is around $\sim 10^3$ TeV (in contrast with LISA, around ~ 10 TeV, and LIGO/Virgo, around $\sim 10^5$ TeV). (ii) Backgrounds of astrophysical origin, produced by supernovae, magnetars, or the inspiral and merger of compact objects (NSs or BHs). Depending on the event rate of these astrophysical GW sources there may create a GW background overlapping the sensitivity band of ELGAR.

3.7. Observing type Ia supernovae

Another source of interest at low frequencies is represented by the type Ia supernova events, expected to emit GWs and neutrinos [171] at frequencies in the gap between terrestrial large optical interferometers and the space detector LISA, as shown in figure 12, where we plot the range of signal strengths for galactic sources.
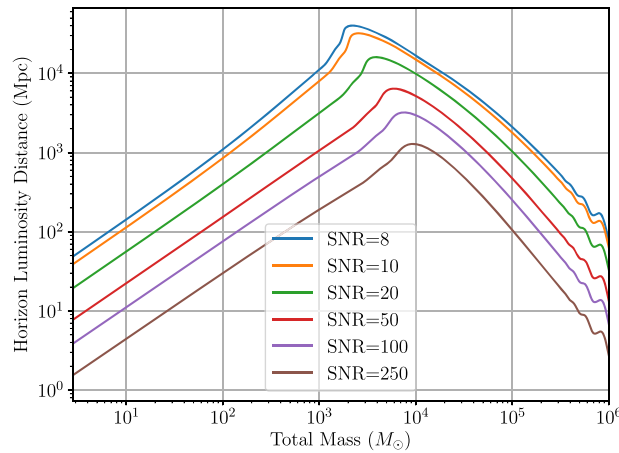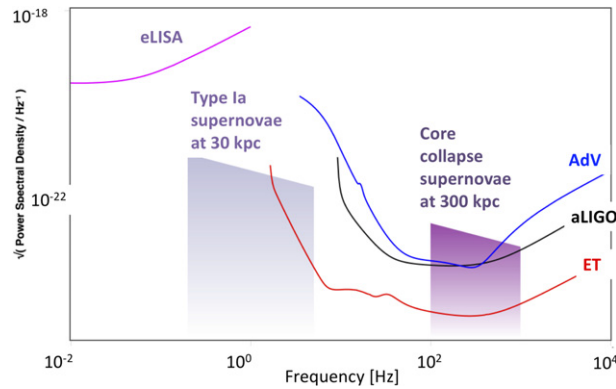
Figure 11. The plot shows the horizon luminosity distance (in logarithmic scale) for ELGAR detections of CBC events in terms of the total mass in the source frame (expressed in units of the Sun mass) for six different SNR detection thresholds (5, 8, 10, 20, 50, and 100).

Figure 12. Type Ia and type II supernovae signal spectra, plotted against detector sensitivities. Figure obtained using the GWplotter tool [130].

Again, these are signals potentially accessible for a detector with sensitivities close to $10^{-21}\,\mathrm{Hz}^{-1/2}$, exactly as type II (core-collapse) galactic supernovae are potentially accessible to LIGO and Virgo. Type Ia supernovae are about as frequent as core-collapse ones, with a frequency in our Galaxy about one per hundred years; therefore the chances for detection are relatively modest, since the odds of detecting events in other galaxies are very unfavourable. Yet, like is the case for core-collapse supernovae, even the detection of a single event could provide a wealth of information on the detonation mechanism [171].

3.8. Multimessenger and multiband GW astronomy with ELGAR

Following the detections of the LIGO and Virgo detectors, we expect that several astrophysical sources of GW transient signals will also emit electromagnetic (and possibly neutrino)

counterpart signals [172, 173] that may detected by GW detectors, in particular by ELGAR. These counterparts (including cosmic rays) will be crucial to maximize the discovery potential of GW detectors, providing a complementary knowledge of astrophysical GW events and the emission mechanisms. The main candidate for electromagnetic counterparts in the case of ELGAR will be binary systems containing an NS which may give rise to the emission of GRBs. In the case of ELGAR, BNSs will not merge inside the band, so we are looking at IMRIs containing an NS.

On the other hand, there are sources of GWs that can be observed in two different bands of the GW spectrum by two different observatories at different times. This has already been suggested between the high-frequency and low-frequency band [10], in the sense that the coalescence of BBHs may be seen before by an observatory like LISA in the frequency band, specially if the masses of these BHs is at the high-end of what LIGO has been observing, as in the first detection of GWs [1]. With LISA observations we can determine the time of coalescence and inform ground-based detectors operating at higher frequencies. Examples of this have been already discussed in the previous subsections. Given that ELGAR is between the low- and high-frequency bands, we have two different possibilities of multiband detections where ELGAR could take part. ELGAR could detect binaries previously detected at the low-frequency band and also binaries that later will be detected by high-frequency detectors (either second-generation ones like LIGO [8], Virgo [9], and KAGRA or third-generation ones like ET [12] or cosmic explorer (CE) [174]).

3.9. Fundamental physics with ELGAR

GWs offer many different ways of doing fundamental physics [175, 176]. We can distinguish different types of questions that we can address with GWs depending on the system we are looking at and the assumptions we make about the systems itself. For instance, if we distinguish between the generation and propagation of the GWs we can see that different types of physics can influence these physical processes and hence they have a very different impact in the waveforms of the radiation emitted. If we look at the propagation of GWs coming from distant sources we can test different types of what we can call fundamental physics: tests of possible violations of Lorentz invariance; test of the existence of extra polarizations of GWs; to bounds on a hypothetical graviton mass (our best estimate, $m_g < 7.7 \times 10^{-23}$ eV/c^2, comes from gravitational-wave observations [177, 178]); tests of parity violations, etc. This type of new physics is usually associated with different theories that predict the presence of extra degrees of freedom, either coming from low-energy limit of quantum gravity theories or from phenomenological models inspired by quantum gravity.

On the other hand, by looking at the late inspiral, merger and ringdown of compact binaries including BHs we can perform tests of the nature of compact objects (in particular of the no-hair conjecture for BHs) and also of the most non-linear and dynamical (radiative) regime of general relativity, not accessible to other types of observatories. We can also investigate whether certain modifications of general relativity are correct and/or put bounds on them. The late inspiral and merger require the use of numerical relativity or precise perturbative methods (like the effective-one-body approach that incorporates information from post-Newtonian theory, BH perturbation theory, and numerical relativity) and allow for tests of the nature of the compact objects and the theory of gravity. If these binary systems involve neutron stars we can also try to constraint the possible equation of state, which is currently not known, and which can tell us about properties of matter and high-energy physics interactions. In the case of BH binaries we can also put bounds on exotic horizonless objects proposed as alternatives to BHs (see, e.g. [179]), as for instance boson stars, gravastars, fuzzballs, etc. Also, the final ringdown when the

deformed BH from the coalescence relaxes to its equilibrium state (a Kerr BH assuming general relativity and the validity of the no-hair conjecture) via damped oscillations, the quasi-normal modes, can allow us to perform fine tests of the no hair conjecture. The idea is simple, the quasi-normal modes are determined by the characteristic frequency of the oscillations and the characteristic damping time. These in turn have been precisely computed in general relativity (and in other alternative theories) for BHs and some alternatives to BHs. Then, we can make as many tests as different quasinormal mode frequencies and damping times are we able to estimate from the GW signal.

Another test of the nature of compact objects and gravity can come from the detections of IMRIs with ELGAR. This goes in the line of what has already been proposed for EMRIs and space-based detectors like LISA (see, e.g. [180–182]). There, it was estimated that during the last year before plunge an EMRI can spend of the order of $\sim q$ cycles (10^5 in the case of a $10 M_\odot$ inspiraling into a $10^6 M_\odot$ MBH). It means that the GWs emitted carry a detailed map of the geometry of the MBH that allows for highly accurate estimations of the main EMRI parameters and even estimations the quadrupole and high-order multipoles [180–182]. For the Kerr metric, there are two sets of gravitational multipole moments, the mass and current (spin) moments, $\{\mathcal{M}_\ell\}_{\ell=0,\dots,\infty}$ and $\{\mathcal{J}_\ell\}_{\ell=0,\dots,\infty}$ respectively, that satisfy the following simple sets of relationships: $\mathcal{M}_\ell + i\mathcal{J}_\ell = M_{\mathrm{BH}}(iJ_{\mathrm{BH}})^\ell$, where M_{BH} and J_{BH} are the mass and spin angular momentum of the MBH. Therefore, if we are able to measure N multipole moments from the GW signal we can perform $N-2$ tests of the geometry of the Kerr BHs. We can extend this program to the case of IMRIs, where the number of cycles in the strong field regime should be of the order of $\sim 10^2$–10^4. In this strong field regime, and in contrast with EMRIs, both the spin–orbit and spin–spin interactions are expected to be important, adding new time scales to the problem and increasing its complexity, both in terms of the structure of gravitational waveforms emitted but also in terms of the modeling required. The EMRI modeling program is today an ongoing program based on the self-force approach that uses BH perturbation theory developments up to second order in the mass ratio. In the case of IMRIs, the smaller mass ratios indicate that perturbation theory alone will not be sufficient and a combination of pertubative methods with numerical relativity will be needed.

Apart from tests on the nature of the most compact objects and the theory of gravity, ELGAR can also contribute to another important problem in fundamental physics: The nature of DM. There have been proposed different ways in which GWs can provide information about DM [183]. We are going to mention here only the ones that are relevant for ELGAR. (i) *Primordial BHs* (PBHs). There are many high-energy models with implications to early-Universe cosmology which predict the formation of BHs less than 1 s after the big bang in the mass range 10^{-16}–$10^6 M_\odot$. PBHs have been proposed by different authors as a candidate for DM, some assuming a single mass scenario and others with a certain mass distribution. Using different types of observations, a number of constraints on the fraction of DM that can be made out of PBHs (see, e.g. [183]) have been derived. On the other hand, there are many different formation scenarios that may be distinguished by inferring the PBH mass spectrum. Each formation scenario may lead to different gravitational-wave signatures. In this sense, it is important to mention that there are two cases of GW detections in which we can be sure that they are not due to BHs of astrophysical origin: the detection of nearby mergers of sub-solar mass BHs with ground-based detectors and BBH mergers at very high redshift ($z > 40$) by future third-generation ground-based detectors like ET and CE (and similarly with space-based detectors like LISA). Even in the case where PBHs do not constitute all of the DM, they can still be connected to DM by forming different types of particle DM mini-halos, whose annihilation may be enhanced giving rise, for instance, to gamma-ray emission. (ii)

Environmental effects. There is the possibility that in the strong-gravity phase of the merger of BHs and/or neutron stars DM may play a role introducing small effects in the emitted gravitational waveforms. The question here is whether we can distinguish the DM environmental effect from other possible environmental effects [184]. (iii) *Exotic binary mergers*. If DM is made out of some kind of particles, it is possible to conceive compact horizonless objects made out of them. The coalescence of these objects may give rise to gravitational waveforms different from those corresponding to BHs and neutron stars. This hypothetical scenario is clearly linked to the program of testing the nature of the most compact objects in the cosmos. (iv) *Non-perturbative DM dynamics*. DM particles may be produced non-perturbatively in the early Universe giving rise to characteristic stochastic GW backgrounds. The question in this case is whether these DM stochastic backgrounds can be distinguished from other stochastic backgrounds, something depends strongly on the shapes of the spectra. (v) *Phase transitions*. They are one of the possible causes of stochastic backgrounds of GWs of primordial original. Given that the standard model of particle physics does not allow for first-order phase transition, detecting a stochastic GW background of this kind means new physics. If such transition is associated with DM particles then we can infer some of the properties from the observations of the GW background.

4. Conclusions

In this paper, we have proposed a European research infrastructure for the observation of GWs in the deciHertz band, between 0.1–10 Hz. ELGAR will be based on the latest developments of quantum physics and will use a geometry based on an 2D array of AIs. These techniques offer important perspectives to limit the impact of seismic noise and NN, which are expected to be major limitations for GW detectors at low frequency. Based on the preliminary design presented in this paper, an ELGAR detector tens of km long could achieve a sensitivity of $3.3 \times 10^{-22}/\sqrt{\text{Hz}}$ at 1.7 Hz, assuming key developments in cold atom technologies mainly related to source parameters and atomic manipulation, but also improvements in NN reduction techniques.

Opening GW detection in the in the deciHertz band, ELGAR will then fill the gap in the GW spectrum between ground-based detectors like Virgo and LIGO (high-frequency band) and space-based detectors like LISA (low-frequency band), where an ambitious science program can be carried out. ELGAR will access a diverse variety of CBC, both from their nature (white dwarfs, NSs, and BHs), their masses (from comparable mass to intermediate mass-ratio binaries), the orbital stage (inspiral, merger, ringdown), and even their presumable origin (stellar origin, globular clusters, early Universe). ELGAR will also be able to detect supernovae core collapse and stochastic backgrounds of GWs, both from astrophysical and early-universe origin. ELGAR should thus be able to answer relevant questions in astrophysics and cosmology, concerning for example the existence of intermediate-mass BHs and their possible formation channels, and the existence of PBHs and the allowed mass ranges. The possibility of detecting with ELGAR the merger and plunge of IMRIs containing neutron stars would make the instrument a key resource for multi-band GW observations and for multimessenger observations. ELGAR will also have an important impact in fundamental physics, particularly for the detection of mergers of intermediate-mass BHs and/or IMRIs with significant SNR. The precise parameter estimation for these sources will enable tests of the no-hair conjecture of BHs and even tests of general relativity and alternative theories. Additionally, ELGAR may also provide information about the nature of DM.

Acknowledgments

ORCID iDs

B Canuel ⬤ https://orcid.org/0000-0002-1378-2334
S Abend ⬤ https://orcid.org/0000-0001-9539-3780
F Badaracco ⬤ https://orcid.org/0000-0001-8553-7904

A Bertoldi https://orcid.org/0000-0002-4839-0947
P Bouyer https://orcid.org/0000-0003-4458-0089
N Gaaloul https://orcid.org/0000-0001-8233-5848
C L Garrido Alzar https://orcid.org/0000-0003-3616-1845
R Geiger https://orcid.org/0000-0003-4678-7139
J Harms https://orcid.org/0000-0002-7332-9806
A Landragin https://orcid.org/0000-0002-2941-4982
B Leykauf https://orcid.org/0000-0002-4630-0602
S Loriani https://orcid.org/0000-0001-6660-960X
M Nofrarias https://orcid.org/0000-0003-1518-2196
P Papadakos https://orcid.org/0000-0001-8926-4229
F Pereira dos Santos https://orcid.org/0000-0003-0659-5028
A Peters https://orcid.org/0000-0001-5538-9250
M Prevedelli https://orcid.org/0000-0002-3136-2392
S Rosat https://orcid.org/0000-0003-4606-2170
A Roura https://orcid.org/0000-0002-8049-8982
D O Sabulsky https://orcid.org/0000-0001-7421-2821
D Schlippert https://orcid.org/0000-0003-2168-1776
L Sidorenkov https://orcid.org/0000-0001-5293-2780
J-N Siemß https://orcid.org/0000-0003-3038-3922
C F Sopuerta https://orcid.org/0000-0002-1779-4447
G M Tino https://orcid.org/0000-0002-7944-9825
A Viceré https://orcid.org/0000-0003-0624-6231
W von Klitzing https://orcid.org/0000-0001-6172-8407
X Zou https://orcid.org/0000-0003-3026-2944

References

[1] Abbott B P *et al* LIGO Scientific Collaboration and Virgo Collaboration 2016 *Phys. Rev. Lett.* **116** 061102
[2] Abramovici A *et al* 1992 *Science* **256** 325–33
[3] Ando S *et al* 2013 *Rev. Mod. Phys.* **85** 1401–20
[4] Abbott B *et al* 2019 *Phys. Rev.* X **9** 031040
[5] Mandel I, Sesana A and Vecchio A 2018 *Class. Quantum Grav.* **35** 054004
[6] Nielsen H and Olesen P 1973 *Nucl. Phys.* B **61** 45–61
[7] Weir D J 2018 *Phil. Trans. R. Soc.* A **376** 20170126
[8] Aasi J *et al* 2015 *Class. Quantum Grav.* **32** 074001
[9] Acernese F *et al* 2014 *Class. Quantum Grav.* **32** 024001
[10] Sesana A 2016 *Phys. Rev. Lett.* **116** 231102
[11] Jennrich O 2009 *Class. Quantum Grav.* **26** 153001
[12] Punturo M *et al* 2010 *Class. Quantum Grav.* **27** 194002
[13] Kuns K A, Yu H, Chen Y and Adhikari R X 2019 Astrophysics and cosmology with a deci-hertz gravitational-wave detector: TianGO (arXiv:1908.06004)
[14] Sedda M A *et al* 2019 The missing link in the gravitational wave astronomy: discoveries waiting in the decihertz range (arXiv:1908.11375)
[15] El-Neaj Y A *et al* 2020 *EPJ Quantum Technol.* **7** 6
[16] Peters A, Chung K Y and Chu S 1999 *Nature* **400** 849–52
[17] Freier C, Hauth M, Schkolnik V, Leykauf B, Schilling M, Wziontek H, Scherneck H G, Müller J and Peters A 2016 *J. Phys.: Conf. Ser.* **723** 012050
[18] Gustavson T L, Bouyer P and Kasevich M A 1997 *Phys. Rev. Lett.* **78** 2046–9
[19] Stockton J K, Takase K and Kasevich M A 2011 *Phys. Rev. Lett.* **107** 133001

[20] Savoie D, Altorio M, Fang B, Sidorenkov L A, Geiger R and Landragin A 2018 *Sci. Adv.* **4** eaau7948

[21] Asenbaum P, Overstreet C, Kovachy T, Brown D D, Hogan J M and Kasevich M A 2017 *Phys. Rev. Lett.* **118** 183602

[22] Rosi G, Sorrentino F, Cacciapuoti L, Prevedelli M and Tino G M 2014 *Nature* **510** 518–21

[23] Bouchendira R, Cladé P, Guellati-Khélifa S, Nez F and Biraben F 2011 *Phys. Rev. Lett.* **106** 287

[24] Dimopoulos S, Graham P W, Hogan J M and Kasevich M A 2007 *Phys. Rev. Lett.* **98** 111102

[25] Aguilera D N *et al* 2014 *Class. Quantum Grav.* **31** 115010

[26] Schlippert D, Hartwig J, Albers H, Richardson L L, Schubert C, Roura A, Schleich W P, Ertmer W and Rasel E M 2014 *Phys. Rev. Lett.* **112** 203002

[27] Zhou L *et al* 2015 *Phys. Rev. Lett.* **115** 3

[28] Rosi G, D'Amico G, Cacciapuoti L, Sorrentino F, Prevedelli M, Zych M, Brukner Ĉ and Tino G M 2017 *Nat. Commun.* **8** 15529

[29] Overstreet C, Asenbaum P, Kovachy T, Notermans R, Hogan J M and Kasevich M A 2018 *Phys. Rev. Lett.* **120** 183604

[30] Burrage C, Copeland E J and Hinds E 2015 *J. Cosmol. Astropart. Phys.* JCAP03(2015)042

[31] Jaffe M, Haslinger P, Xu V, Hamilton P, Upadhye A, Elder B, Khoury J and Müller H 2017 *Nat. Phys.* **13** 938–42

[32] Sabulsky D, Dutta I, Hinds E, Elder B, Burrage C and Copeland E J 2019 *Phys. Rev. Lett.* **123** 061102

[33] Bongs K, Holynski M, Vovrosh J, Bouyer P, Condon G, Rasel E, Schubert C, Schleich W P and Roura A 2019 *Nat. Rev. Phys.* **1** 731–9

[34] Trimeche A *et al* 2019 *Class. Quantum Grav.* **36** 215004

[35] De Angelis M, Bertoldi A, Cacciapuoti L, Giorgini A, Lamporesi G, Prevedelli M, Saccorotti G, Sorrentino F and Tino G M 2009 *Meas. Sci. Technol.* **20** 022001

[36] Ménoret V, Vermeulen P, Moigne N L, Bonvalot S, Bouyer P, Landragin A and Desruelle B 2018 *Sci. Rep.* **8** 12300

[37] Bidel Y, Zahzam N, Blanchard C, Bonnin A, Cadoret M, Bresson A, Rouxel D and Lequentrec-Lalancette M F 2018 *Nat. Commun.* **9** 65

[38] Kasevich M A and Dubetsky B 2006 Kinematic sensors employing atom interferometer phases *US Patent* 7317184B2

[39] Barrett B, Cheiney P, Battelier B, Napolitano F and Bouyer P 2019 *Phys. Rev. Lett.* **122** 043604

[40] Chaibi W, Geiger R, Canuel B, Bertoldi A, Landragin A and Bouyer P 2016 *Phys. Rev. D* **93** 021101

[41] Chung K Y, Chiow S W, Herrmann S, Chu S and Müller H 2009 *Phys. Rev. D* **80** 016002

[42] Diósi L 1987 *Phys. Lett.* A **120** 377–81

[43] Penrose R 1996 *Gen. Relativ. Gravit.* **28** 581–600

[44] Pikovski I, Zych M, Costa F and Brukner Ĉ 2015 *Nat. Phys.* **11** 668–72

[45] Roura A 2020 *Phys. Rev.* X **10** 021014

[46] Pfister H 2007 *Gen. Relativ. Gravit.* **39** 1735–48

[47] Cronin A D, Schmiedmayer J and Pritchard D E 2009 *Rev. Mod. Phys.* **81** 1051–129

[48] Storey P and Cohen-Tannoudji C 1994 *J. Physique II* **4** 1999–2027

[49] Kasevich M and Chu S 1991 *Phys. Rev. Lett.* **67** 181

[50] Peters A, Chung K Y and Chu S 2001 *Metrologia* **38** 25–61

[51] Dimopoulos S, Graham P, Hogan J, Kasevich M and Rajendran S 2008 *Phys. Rev. D* **78** 122002

[52] Wieman C E, Pritchard D E and Wineland D J 1999 *Rev. Mod. Phys.* **71** S253–62

[53] Bertoldi A *et al* 2006 *Eur. Phys. J. D* **40** 271–9

[54] Denschlag J H, Simsarian J E, Häffner H, McKenzie C, Browaeys A, Cho D, Helmerson K, Rolston S L and Phillips W D 2002 *J. Phys. B: At. Mol. Opt. Phys.* **35** 3095–110

[55] Dickerson S M, Hogan J M, Sugarbaker A, Johnson D M S and Kasevich M A 2013 *Phys. Rev. Lett.* **111** 083001

[56] Canuel B *et al* 2020 Technologies for the ELGAR large scale atom interferometer array (arXiv:2007.04014)

[57] Dutta I, Savoie D, Fang B, Venon B, Garrido Alzar C L, Geiger R and Landragin A 2016 *Phys. Rev. Lett.* **116** 183003

[58] Canuel B *et al* 2006 *Phys. Rev. Lett.* **97** 010402

[59] McDonald G D, Kuhn C C N, Bennetts S, Debs J E, Hardman K S, Johnsson M, Close J D and Robins N P 2013 *Phys. Rev.* A **88** 053620

[60] Bouchendira R, Cladé P, Guellati-Khélifa S, Nez F and Biraben F 2011 *Phys. Rev. Lett.* **106** 080801

[61] Rocco E, Palmer R N, Valenzuela T, Boyer V, Freise A and Bongs K 2014 *New J. Phys.* **16** 093046

[62] Cheinet P, Canuel B, Pereira Dos Santos F, Gauguet A, Yver-Leduc F and Landragin A 2008 *IEEE Trans. Instrum. Meas.* **57** 1141

[63] Lévèque T 2010 Development of a high sensitivity cold atom gyroscope based on a folded geometry PhD Thesis Université Pierre et Marie Curie, Paris VI https://tel.archives-ouvertes.fr/tel-00532789v2

[64] Canuel B *et al* 2018 *Sci. Rep.* **8** 14064

[65] Canuel B *et al* 2016 *Proc. SPIE* **9900** 990008

[66] Fiorucci D, Harms J, Barsuglia M, Fiori I and Paoletti F 2018 *Phys. Rev.* D **97** 062003

[67] Junca J *et al* 2019 *Phys. Rev.* D **99** 104026

[68] Gaffet S 2019 The LSBB underground research laboratory: a unique facility for fundamental and applied low background inter-disciplinary ground and underground science and technology Rencontres scientifiques et techniques RESIF 2019 https://hal.archives-ouvertes.fr/hal-02415351

[69] Naticchioni L *et al* 2020 *J. Phys.: Conf. Ser.* **1468** 012242

[70] Simeone M 2018 The ARIA project: production of depleted argon for the DarkSide experiment https://zenodo.org/record/1239128

[71] Graham P W, Hogan J M, Kasevich M A and Rajendran S 2016 *Phys. Rev.* D **94** 104022

[72] Marzlin K P and Audretsch J 1996 *Phys. Rev.* A **53** 312

[73] Hogan J M *et al* 2011 *Gen. Relativ. Gravit.* **43** 1953–2009

[74] Kleinert S, Kajari E, Roura A and Schleich W P 2015 *Phys. Rep.* **605** 1

[75] Schubert C, Schlippert D, Abend S, Giese E, Roura A, Schleich W P, Ertmer W and Rasel E M 2019 Scalable, symmetric atom interferometer for infrasound gravitational wave detection (arXiv:1909.01951)

[76] Roura A 2017 *Phys. Rev. Lett.* **118** 160401

[77] D'Amico G, Rosi G, Zhan S, Cacciapuoti L, Fattori M and Tino G 2017 *Phys. Rev. Lett.* **119** 253201

[78] Bertoldi A, Minardi F and Prevedelli M 2019 *Phys. Rev.* A **99** 033619

[79] Giltner D, McGowan R and Lee S 1995 *Phys. Rev. Lett.* **75** 2638

[80] Peik E, Ben Dahan M, Bouchoule S, Castin Y and Salomon C 1997 *Phys. Rev.* A **55** 2989

[81] Cadoret M, de Mirandes E, Cladé P, Guellati-Khélifa S, Schwob C, Nez F, Julien L and Biraben F 2008 *Phys. Rev. Lett.* **101** 230801

[82] Müller H, Chiow S W, Long Q, Herrmann S and Chu S 2008 *Phys. Rev. Lett.* **100** 180405

[83] Jaffe M, Xu V, Haslinger P, Müller H and Hamilton P 2018 *Phys. Rev. Lett.* **121** 040402

[84] McGuirk J, Snadden M and Kasevich M 2000 *Phys. Rev. Lett.* **85** 4498

[85] Gebbe M *et al* 2019 Twin-lattice atom interferometry (arXiv:1907.08416)

[86] Müller H, Chiow S W and Chu S 2008 *Phys. Rev.* A **77** 023609

[87] Müller H, Chiow S W, Herrmann S and Chu S 2009 *Phys. Rev. Lett.* **102** 240403

[88] Pagel Z *et al* 2019 Bloch beamsplitters and dual-lattice methods for atom interferometry (arXiv:1907.05994)

[89] Ahlers H *et al* 2016 *Phys. Rev. Lett.* **116** 173601

[90] Kovachy T, Chiow S W and Kasevich M 2012 *Phys. Rev.* A **86** 011606

[91] Graham P W, Hogan J M, Kasevich M A and Rajendran S 2013 *Phys. Rev. Lett.* **110** 171102

[92] Hu L, Poli N, Salvi L and Tino G 2017 *Phys. Rev. Lett.* **119** 263601

[93] Rudolph J, Wilkason T, Nantel M, Swan H, Holland C M, Jiang Y, Garber B E, Carman S P and Hogan J M 2020 *Phys. Rev. Lett.* **124** 083604

[94] Hogan J M and Kasevich M A 2016 *Phys. Rev.* A **94** 033632

[95] Loriani S *et al* 2019 *New J. Phys.* **21** 063030

[96] Rudolph J 2016 Matter-wave optics with Bose-Einstein condensates in microgravity PhD Thesis Gottfried Wilhelm Leibniz Universität Hannover

[97] Kovachy T, Hogan J M, Sugarbaker A, Dickerson S M, Donnelly C A, Overstreet C and Kasevich M A 2015 *Phys. Rev. Lett.* **114** 143004

[98] Parker R H, Yu C, Zhong W, Estey B and Müller H 2018 *Science* **360** 191–5

[99] Pezzè L, Smerzi A, Oberthaler M K, Schmied R and Treutlein P 2018 *Rev. Mod. Phys.* **90** 035005

[100] Hosten O, Engelsen N J, Krishnakumar R and Kasevich M A 2016 *Nature* **529** 505–8

[101] Cox K C, Greve G P, Weiner J M and Thompson J K 2016 *Phys. Rev. Lett.* **116** 093602

[102] Stephens M, Saulson P and Kovalik J 1991 *Rev. Sci. Instrum.* **62** 924–32

[103] Accadia T *et al* 2011 *J. Low Freq. Noise Vib. Act. Contr.* **30** 63–79
[104] Winterflood J, Barber T and Blair D G 2002 *Class. Quantum Grav.* **19** 1639–45
[105] Hosain M, Sirr A, Ju L and Blair D 2012 *Rev. Sci. Instrum.* **83** 085108
[106] Garoi F, Winterflood J, Ju L, Jacob J and Blair D G 2003 *Rev. Sci. Instrum.* **74** 3487–91
[107] Barriga P, Dumas J C, Woolley A A, Zhao C and Blair D G 2009 *Rev. Sci. Instrum.* **80** 114501
[108] Saulson P R, Stebbins R T, Dumont F D and Mock S E 1994 *Rev. Sci. Instrum.* **65** 182–91
[109] Chalapathy R and Chawla S 2019 Deep learning for anomaly detection: a survey (arXiv:1901.03407)
[110] Yang X, Ramesh P, Chitta R, Madhvanath S, Bernal E A and Luo J 2017 Deep multimodal representation learning from temporal data *Proc. of the IEEE Conf. on Computer Vision and Pattern Recognition* pp 5447–55
[111] Abbott B P *et al* LIGO Scientific, Virgo 2018 *Phys. Rev.* X **9** 031040
[112] Hulse R A and Taylor J H 1975 *Astrophys. J.* **195** L51–3
[113] Weisberg J M and Huang Y 2016 *Astrophys. J.* **829** 55
[114] Manchester R N, Hobbs G B, Teoh A and Hobbs M 2005 *Astron. J.* **129** 1993
[115] Abadie J *et al* LIGO Scientific Collaboration and Virgo Collaboration 2010 *Class. Quantum Grav.* **27** 173001
[116] Abbott B P *et al* LIGO Scientific Collaboration and Virgo Collaboration 2017 *Phys. Rev. Lett.* **119** 161101
[117] LIGO Scientific Collaboration and Virgo Collaboration 2017 Fermi Gamma-ray Burst Monitor, and INTEGRAL *Astrophys. J. Lett.* **848** L13
[118] Blinnikov S I, Novikov I D, Perevodchikova T V and Polnarev A G 1984 *Sov. Astron. Lett.* **10** 177 (arXiv:1808.05287)
[119] Amaro-Seoane P *et al* 2017 Laser interferometer space antenna (arXiv:1702.00786)
[120] Armano M *et al* 2016 *Phys. Rev. Lett.* **116** 231101
[121] Armano M *et al* 2018 *Phys. Rev. Lett.* **120** 061101
[122] Armano M *et al* 2019 *Phys. Rev. Lett.* **123** 111101
[123] Seoane P A *et al* eLISA 2013 The gravitational universe (arXiv:1305.5720)
[124] Desvignes G *et al* EPTA 2016 *Mon. Not. R. Astron. Soc.* **458** 3341–80
[125] Arzoumanian Z *et al* 2018 NANOGrav *Astrophys. J. Suppl.* **235** 37
[126] Reardon D J *et al* and PPTA 2016 *Mon. Not. R. Astron. Soc.* **455** 1751–69
[127] Perera B B P *et al* IPTA 2019 *Mon. Not. R. Astron. Soc.* accepted
[128] Abbott B P *et al* LIGO Scientific Collaboration and Virgo Collaboration 2019 *Astrophys. J. Lett.* **882** L24
[129] Sathyaprakash B *et al* 2012 *Class. Quantum Grav.* **29** 124013
[130] Moore C J, Cole R H and Berry C P L 2015 *Class. Quantum Grav.* **32** 015014
[131] Kormendy J and Ho L C 2013 *Annu. Rev. Astron. Astrophys.* **51** 511–653
[132] Mezcua M 2017 *Int. J. Mod. Phys.* D **26** 1730021
[133] Amaro-Seoane P and Freitag M 2006 *Astrophys. J.* **653** L53–6
[134] Amaro-Seoane P, Miller M C and Freitag M 2009 *Astrophys. J.* **692** L50–3
[135] Amaro-Seoane P, Eichhorn C, Porter E K and Spurzem R 2010 *Mon. Not. R. Astron. Soc.* **401** 2268–84
[136] Gürkan M A, Fregeau J M and Rasio F A 2006 *Astrophys. J.* **640** L39–42
[137] Fregeau J M, Larson S L, Miller M C, O'Shaughnessy R and Rasio F A 2006 *Astrophys. J.* **646** L135–8
[138] Peters P C 1964 *Phys. Rev.* **136** B1224–32
[139] Amaro-Seoane P and Santamaría L 2010 *Astrophys. J.* **722** 1197–206
[140] Amaro-Seoane P 2018 *Living Rev. Relativ.* **21** 4
[141] Amaro-Seoane P, Gair J R, Pound A, Hughes S A and Sopuerta C F 2015 *J. Phys.: Conf. Ser.* **610** 012002
[142] Amaro-Seoane P, Gair J R, Freitag M, Miller M C, Mandel I, Cutler C J and Babak S 2007 *Class. Quantum Grav.* **24** R113–69
[143] Brown D A, Brink J, Fang H, Gair J R, Li C, Lovelace G, Mandel I and Thorne K S 2007 *Phys. Rev. Lett.* **99** 201102
[144] Rodriguez C L, Mandel I and Gair J R 2012 *Phys. Rev.* D **85** 062002
[145] Hansen R O 1972 *Phys. Rev.* D **5** 1021–3
[146] Quinlan G D and Shapiro S L 1989 *Astrophys. J.* **343** 725–49
[147] Kocsis B, Gáspár M E and Márka S 2006 *Astrophys. J.* **648** 411–29

[148] Mandel I, Brown D A, Gair J R and Miller M C 2008 *Astrophys. J.* **681** 1431–47
[149] O'Leary R, Kocsis B and Loeb A 2009 *Mon. Not. R. Astron. Soc.* **395** 2127–46
[150] Lee W H, Ramirez-Ruiz E and van de Ven G 2010 *Astrophys. J.* **720** 953–75
[151] Hong J and Lee H M 2015 *Mon. Not. R. Astron. Soc.* **448** 754–70
[152] Konstantinidis S, Amaro-Seoane P and Kokkotas K D 2013 *Astron. Astrophys.* **557** A135
[153] Campanelli M, Lousto C O, Marronetti P and Zlochower Y 2006 *Phys. Rev. Lett.* **96** 111101
[154] Baker J G, Centrella J, Choi D I, Koppitz M, van Meter J R and Miller M C 2006 *Astrophys. J.* **653** L93–6
[155] González J A, Sperhake U, Brügmann B, Hannam M and Husa S 2007 *Phys. Rev. Lett.* **98** 091101
[156] Leigh N W C, Lützgendorf N, Geller A M, Maccarone T J, Heinke C and Sesana A 2014 *Mon. Not. R. Astron. Soc.* **444** 29–42
[157] MacLeod M, Trenti M and Ramirez-Ruiz E 2016 *Astrophys. J.* **819** 70
[158] Haster C J, Antonini F, Kalogera V and Mandel I 2016 *Astrophys. J.* **832** 192
[159] Hild S, Abernathy M, Acernese F, Amaro-Seoane P *et al* 2011 *Class. Quantum Grav.* **28** 094013
[160] Amaro-Seoane P 2018 *Phys. Rev. D* **98** 063018
[161] Amaro-Seoane P and Chen X 2016 *Mon. Not. R. Astron. Soc.* **458** 3075–82
[162] Chen X and Amaro-Seoane P 2017 *Astrophys. J.* **842** L2
[163] Chen H Y 2016 Distance tool https://github.com/hsinyuc/distancetool
[164] Rollins J and Creighton J 2017 Gw detector inspiral range calculation tools https://git.ligo.org/gwinc/inspiral-range
[165] Chen H Y, Holz D E, Miller J, Evans M, Vitale S and Creighton J 2017 Distance measures in gravitational-wave astrophysics and cosmology (arXiv:1709.08079)
[166] LIGO Scientific Collaboration 2018 *LIGO Algorithm Library—LALSuite Free Software (GPL)* https://10.7935/GT1W-FZ16
[167] Khan S, Husa S, Hannam M, Ohme F, Pürrer M, Jimenez Forteza X and Bohé A 2016 *Phys. Rev. D* **93** 044007
[168] Ade P A R *et al* Planck 2016 *Astron. Astrophys.* **594** A13
[169] Christensen N 2019 *Rep. Prog. Phys.* **82** 016903
[170] Caprini C and Figueroa D G 2018 *Class. Quantum Grav.* **35** 163001
[171] Seitenzahl I R *et al* 2015 *Phys. Rev. D* **92** 124013
[172] Sathyaprakash B S *et al* 2019 Multimessenger universe with gravitational waves from binaries (arXiv:1903.09277)
[173] Fan X and Hendry M 2015 Multimessenger astronomy (arXiv:1509.06022)
[174] Reitze D *et al* 2019 Cosmic explorer: The U.S. contribution to gravitational-wave astronomy beyond LIGO (arXiv:1907.04833)
[175] Barack L *et al* 2019 *Class. Quantum Grav.* **36** 143001
[176] Sathyaprakash B S *et al* 2019 Extreme gravity and fundamental physics (arXiv:1903.09221)
[177] Abbott B P *et al* LIGO Scientific Collaboration and Virgo Collaboration 2018 *Phys. Rev. Lett.* **121** 129902
[178] Abbott B P *et al* LIGO Scientific Collaboration and Virgo Collaboration 2018 *Phys. Rev. Lett.* **121** 129901
[179] Cardoso V and Pani P 2019 *Living Rev. Relativ.* **22** 4
[180] Babak S *et al* 2017 *Phys. Rev. D* **95** 103012
[181] Berry C P L, Hughes S A, Sopuerta C F, Chua A J K, Heffernan A, Holley-Bockelmann K, Mihaylov D P, Miller M C and Sesana A 2019 The unique potential of extreme mass-ratio inspirals for gravitational-wave astronomy (arXiv:1903.03686)
[182] Sopuerta C F 2010 *A Roadmap to Fundamental Physics from LISA EMRI Observations* (GW Notes vol 4) ed P Amaro-Seoane and B F Schutz (Max-Planck-Institut für Gravitationsphysik: Am Mühlenberg 1 14476 Potsdam Germany) pp 3–47
[183] Bertone G *et al* 2019 Gravitational wave probes of dark matter: challenges and opportunities (arXiv:1907.10610)
[184] Barausse E, Cardoso V and Pani P 2014 *Phys. Rev. D* **89** 104059